RESEARCH ARTICLE

WILEY

A comparative study of micromorphic gradient-extensions for anisotropic damage at finite strains

Tim van der Velden | Tim Brepols | Stefanie Reese | Hagen Holthusen

Institute of Applied Mechanics, RWTH Aachen University, Aachen, Germany

Correspondence

Tim van der Velden, Institute of Applied Mechanics, RWTH Aachen University, Mies-van-der-Rohe-Str. 1, D-52074, Aachen, Germany.

Email:

tim.van.der.velden@ifam.rwth-aachen.de

Funding information

German Research Foundation, Grant/Award Numbers: 453715964 (RE 1057/51-1), 417002380 (CRC 280 - A01), 453596084 (CRC 339 - B05)

Abstract

Modern inelastic material model formulations rely on the use of tensor-valued internal variables. When inelastic phenomena include softening, simulations of the former are prone to localization. Thus, an accurate regularization of the tensor-valued internal variables is essential to obtain physically correct results. Here, we focus on the regularization of anisotropic damage at finite strains. Thus, a flexible anisotropic damage model with isotropic, kinematic, and distortional hardening is equipped with three gradient-extensions using a full and two reduced regularizations of the damage tensor. Theoretical and numerical comparisons of the three gradient-extensions yield excellent agreement between the full and the reduced regularization based on a volumetric-deviatoric regularization using only two nonlocal degrees of freedom.

KEYWORDS

anisotropic damage, gradient-extension, localization, micromorphic approach

1 | INTRODUCTION

Motivation. The prediction of complex material phenomena is, nowadays, based on inelastic material models with tensor-valued internal variables for the description of for example, plasticity, viscoelasticity, anisotropic damage, or growth. Yet, finite element simulations of inelastic phenomena without a regularization method suffer from the occurrence of localization when modeling softening in for example, plasticity and damage de Borst et al., or viscoelasticity Steif et al. Analogously to Poh et al. for small strain plasticity, this work is concerned with the open research question of choosing a regularization for tensor-valued internal variables and focuses on the specific inelastic phenomenon of anisotropic damage. It is well-established that regularizations in the form of gradient-extensions can remedy mesh dependence due to damage softening and restore the ellipticity of the boundary value problem, while the crack localizes in a band of finite width (e.g., Friedlein et al. and the literature cited therein). Here, the first objective is the identification of an efficient gradient-extension for anisotropic damage with a reduced number of nonlocal variables to decrease the size

This paper is dedicated to Robert L. Taylor on the occasion of his 90th birthday and his outstanding contributions to the finite element method. All authors became dedicated devotees of his software FEAP. utan,,1!

Stefanie Reese will never forget Bob's visit to Darmstadt in the nineties and his great explanation of the Hu-Washizu functional. After that, we had many more contacts in Berkeley and at conferences which were always very pleasant and enlightening. We are still using FEAP, from version 3 in the last century to 8.6 today. Bob, we wish you some more versions to come.

This is an open access article under the terms of the Creative Commons Attribution-NonCommercial-NoDerivs License, which permits use and distribution in any medium, provided the original work is properly cited, the use is non-commercial and no modifications or adaptations are made.

© 2024 The Author(s). *International Journal for Numerical Methods in Engineering* published by John Wiley & Sons Ltd.

of the global system of equations. The second objective is to ensure that the physical response remains unaltered when reducing the number of nonlocal variables.

Anisotropic damage modeling. Various modeling methodologies have evolved to describe the induced anisotropy due to material degradation. Formulations based on a split of the volumetric (isotropic) and deviatoric (anisotropic) material response that are separately degraded by two scalar damage variables may be found in for example, Carol et al.⁵ and Leukart and Ramm.⁶ Microplane models, see for example, Carol et al.⁷ and Kuhl et al.,⁸ project the macroscopic strain state onto different material planes, where unidirectional constitutive laws are evaluated, and afterwards obtain the macroscopic material response by a homogenization process (cf. Leukart and Ramm⁶). A multiplicative split of the deformation gradient into elastic and damage related components is used by for example, Voyiadjis and Park,⁹ Schütte and Bruhns,¹⁰ and Dorn and Wulfinghoff,¹¹ where the latter consider the inelastic part to consist out of a normal crack and a shear crack contribution. An effective or fictitious undamaged configuration is introduced by for example, Menzel et al.,¹² Langenfeld and Mosler,¹³ and Sprave and Menzel¹⁴ to formulate the modeling equations. Finally, anisotropic damage can be interpreted as an evolving structural tensor, see for example, Desmorat et al.¹⁵ (whose localization properties were investigated in Jirásek and Suárez¹⁶), Badreddine et al.,¹⁷ Desmorat,¹⁸ Fassin et al.,¹⁹ Fassin et al.,²⁰ Reese et al.,²¹ Hegde and Mulay,²² and Holthusen et al.,²³ which is also the approach followed in this work. Moreover, the employed damage model serves for the modeling of brittle damage of initially isotropic materials, which is applicable for material classes like concrete, glass, or ceramics.

Regularization techniques. To remedy the mesh dependence and ensure a correct modeling of the crack localization, different approaches can be pursued to account for a nonlocal behavior. Spatial averaging techniques for a specific quantity are employed in nonlocal integral-type formulations, see for example, Pijaudier-Cabot and Bažant²⁴ for a spatial average of the damage driving variable, Bažant and Pijaudier-Cabot²⁵ for a spatial average of the damage variable, and Bažant and Jirásek²⁶ for an overview of nonlocal integral-type formulations. Viscous regularization approaches may be found in for example, Needleman,²⁷ Geers et al.,²⁸ Niazi et al.,²⁹ Langenfeld et al.³⁰ and peridynamics based formulations that are inherently nonlocal in for example, Silling,³¹ Javili et al.,³² and Laurien et al.³³

Gradient-extended models provide another effective regularization method that incorporate the gradient of a (local) quantity into the formulation. In for example, Peerlings et al.,³⁴ the gradient of the equivalent strain and, in de Borst et al.,³⁵ the gradient of an internal variable are considered. Moreover, the gradient-extension of an anisotropic microplane damage model is presented in Kuhl et al.⁸ A decisive advancement for gradient-extended material models with respect to their straightforward model incorporation is associated with the works of Dimitrijevic and Hackl,³⁶ Dimitrijevic and Hackl³⁷ and Forest,^{38,39} who introduce a nonlocal counterpart for the local variable, which is to be regularized. The gradient effects act on the nonlocal field and the coupling between the local variable and its nonlocal counterpart is achieved by a penalty approach. Thereby, the local material model formulation is equipped with an additional driving force, but remains otherwise unaltered, which is from the authors' point of view an elegant incorporation of the nonlocal character.

Current and future works. The search for efficient gradient-extension of tensor-valued internal variables is an active field of research and not restricted to anisotropic damage, but also for example, plasticity still an open question. After the works of for example, Wulfinghoff and Böhlke⁴⁰ and Wulfinghoff et al.⁴¹ for strain gradient plasticity, novel scalar-based gradient plasticity models are presented in Jebahi and Forest,⁴² Abatour et al.,⁴³ and Abatour and Forest.⁴⁴ Further, Friedlein et al.⁴ compare different gradient-extensions in the logarithmic strain space for plasticity coupled to damage. Moreover, gradient-extensions for fiber-reinforced materials are presented by for example, Holthusen et al.,⁴⁵ Poggenpohl et al.⁴⁶ and the search for gradient-extended scale-transitions at severe material softening by Poggenpohl et al.⁴⁷ In Langenfeld et al.,⁴⁸ three different regularization concepts for brittle damage are compared and, in Sprave and Menzel,¹⁴ gradient-extensions for anisotropic damage and plasticity at finite strains are investigated.

Following the search for a reduced and effective gradient-extension, the model should then be incorporated into structural elements (e.g., Aldakheel et al.,⁴⁹ Barfusz et al.,^{50,51} and Kikis et al.⁵²) to avoid locking and be combined with a multiphysical framework (e.g., Dittmann et al.,⁵³ Sarkar et al.,⁵⁴ and van der Velden et al.^{55,56}) for holistic production and process simulations. Furthermore, an incorporation of the reduced gradient-extension into the novel iCANN-framework of Holthusen et al.⁵⁷ is aspired.

Outline of the work. In Section 2, the constitutive modeling framework of the anisotropic damage model is elaborated for a general gradient-extension. Then, in Section 3, three specific gradient-extensions are motivated and compared theoretically. Thereafter, in Section 4, the three gradient-extended models are applied to four structural examples and

compared with respect to the structural responses and the resulting damage patterns. Finally, a conclusion is presented in Section 5.

Notational conventions. In this work, italic characters a, A denote scalars and zeroth-order tensors and bold-face italic characters b, B refer to first- and second-order tensors. The operators $\mathrm{Div}(\bullet)$ and $\mathrm{Grad}(\bullet)$ denote the divergence and gradient operation of a quantity with respect to the reference configuration. A · defines the single contraction and a : the double contraction of two tensors. The time derivative of a quantity is given by (\bullet) .

2 | CONSTITUTIVE MODELING

In this Section 2, we briefly present the brittle model version of Holthusen et al.²³ without specification of its gradient-extension. The core and novelty part of this article, that is, the choice and comparison of different gradient-extensions, is discussed in detail in Section 3.

2.1 | Strong and weak forms

The gradient-extension in this work is incorporated following the micromorphic approach of Forest 38,39 using a nonlocal micromorphic tuple (see Holthusen et al. 23). Thus, the balance of linear momentum, stated in the reference configuration, reads

$$Div(FS) + f_0 = 0 \quad \text{in } \Omega_0, \tag{1}$$

$$FS \cdot \mathbf{n}_0 = \mathbf{t}_0 \quad \text{on } \Gamma_{t0}, \tag{2}$$

$$\mathbf{u} = \mathbf{u}' \quad \text{on } \Gamma_{u0},$$
 (3)

and, furthermore, the balance of the micromorphic field reads

$$\operatorname{Div}(\mathbf{\Xi}_{0_{i}} - \mathbf{\Xi}_{0_{e}}) - \boldsymbol{\xi}_{0_{i}} + \boldsymbol{\xi}_{0_{e}} = \mathbf{0} \quad \text{in } \Omega_{0}, \tag{4}$$

$$\left(\mathbf{\Xi}_{0_i} - \mathbf{\Xi}_{0_o}\right) \cdot \mathbf{n}_0 = \boldsymbol{\xi}_{0_o} \quad \text{on } \Gamma_{c0}, \tag{5}$$

$$\overline{\mathbf{d}} = \overline{\mathbf{d}}' \quad \text{on } \Gamma_{\overline{d0}} \tag{6}$$

with the primary variables being the displacement \boldsymbol{u} and the nonlocal micromorphic tuple $\overline{\mathbf{d}}$. Moreover, \boldsymbol{F} denotes the deformation gradient, \boldsymbol{S} the second Piola-Kirchhoff stress, \boldsymbol{f}_0 the mechanical volume forces, \boldsymbol{n}_0 the outward normal vector, \boldsymbol{t}_0 the applied mechanical surface tractions, $\boldsymbol{\xi}_{0_i}$ and $\boldsymbol{\Xi}_{0_i}$ the internal forces related to the micromorphic tuple and its gradient, $\boldsymbol{\xi}_{0_e}$ and $\boldsymbol{\Xi}_{0_e}$ the micromorphic volume forces, and $\boldsymbol{\xi}_{0_e}$ the micromorphic tractions. Boundary conditions for the primary variables are generally denoted by $(\bullet)'$. However, since $\Gamma_{\overline{d}0} = \emptyset$ is employed, for the micromorphic boundary conditions $\Gamma = \Gamma_{\overline{c}0}$ holds.

Using the test functions $\delta \mathbf{u}$ and $\delta \overline{\mathbf{d}}$, the strong forms, Equations (1)–(6), are transferred to their corresponding weak forms under the assumption of a simplified micromorphic balance equation, that is, neglecting external and contact forces as well as Dirichlet boundary conditions for the micromorphic tuple, resulting in

$$g_{u}(\boldsymbol{u}, \overline{\mathbf{d}}, \delta \boldsymbol{u}) := \int_{\Omega_{0}} \boldsymbol{S} : \delta \boldsymbol{E} \, dV - \int_{\Omega_{0}} \boldsymbol{f}_{0} \cdot \delta \boldsymbol{u} \, dV - \int_{\Gamma_{0}} \boldsymbol{t}_{0} \cdot \delta \boldsymbol{u} \, dA = 0, \tag{7}$$

$$g_{\overline{d}}(\boldsymbol{u}, \overline{\mathbf{d}}, \delta \overline{\mathbf{d}}) := \int_{\Omega_0} \xi_{0_i} \cdot \delta \overline{\mathbf{d}} \, dV + \int_{\Omega_0} \Xi_{0_i} : \operatorname{Grad}(\delta \overline{\mathbf{d}}) \, dV = 0.$$
 (8)

Finally, for the linearization and finite element discretization the reader is kindly referred to Holthusen et al.²³

0970207, 0, Downloaded from https://onlinelibrary.wiley.com/doi/10.1002/nme.7580 by Rwth Aachen Hochschulbibliothek, Wiley Online Library on [15/08/2024]. See the Terms and Conditions

2.2 | Kinematics

The constitutive framework is based on logarithmic strains and, thereby, facilitates a physically motivated formulation of the elastic energy contribution that distinguishes between isochoric and volumetric damage mechanisms in the finite strain regime considering the damage growth criterion of Wulfinghoff et al.⁵⁸ Analogously to for example, Miehe et al.,⁵⁹ the logarithmic strain is defined as

$$\boldsymbol{\eta} := \frac{1}{2} \ln(\boldsymbol{C}), \tag{9}$$

where *C* denotes the right Cauchy–Green deformation tensor.

In contrast to the additive split used in finite strain plasticity, see for example, Holthusen et al.²³ for ductile damage with logarithmic strains, which is only exactly valid for coaxial loadings, the consideration of solely brittle damage does not rely on kinematic approximations and, hence, the framework in this work is geometrically exact.

2.3 | Thermodynamically consistent derivation

The model's total Helmholtz free energy ψ is additively split into four contributions

$$\psi\left(\boldsymbol{\eta}, \boldsymbol{D}, \xi_d, \mathbf{d}, \overline{\mathbf{d}}, \operatorname{Grad}(\overline{\mathbf{d}})\right) = \psi_e(\boldsymbol{\eta}, \boldsymbol{D}) + \psi_d(\xi_d) + \psi_h(\boldsymbol{D}) + \psi_{\overline{d}}(\mathbf{d}, \overline{\mathbf{d}}, \operatorname{Grad}(\overline{\mathbf{d}})), \tag{10}$$

where ψ_e represents the elastic energy depending on the strain η and the second-order damage tensor \boldsymbol{D} . Next, ψ_d represents the isotropic damage hardening energy depending on the accumulated damage variable ξ_d . The additional kinematic damage hardening energy ψ_h (cf. Hansen and Schreyer⁶⁰) ensures that the eigenvalues of the damage tensor are limited to a value of one and that complete failure is described by $\boldsymbol{D} = \boldsymbol{I}$ (see Fassin et al.,¹⁹ Fassin et al.,²⁰ and Holthusen et al.²³). Finally, $\psi_{\overline{d}}$ represents the micromorphic energy contribution depending on a general local tuple $\boldsymbol{d} := (d_1, \ldots, d_{n_{\overline{d}}})$, a set of $n_{\overline{d}}$ local invariants formulated in terms of the damage tensor \boldsymbol{D} , and as a corresponding counterpart the nonlocal micromorphic tuple $\overline{\boldsymbol{d}} := (\overline{d}_1, \ldots, \overline{d}_{n_{\overline{d}}})$ and its gradient Grad($\overline{\boldsymbol{d}}$).

Following a general derivation in this section, the specific forms of the energies are presented in Section 2.4. The isothermal Clausius–Duhem inequality including the micromorphic extension reads (cf. Forest^{38,39})

$$-\dot{\psi} + \alpha : \dot{\eta} + \xi_0 \cdot \dot{\overline{\mathbf{d}}} + \Xi_0 : \operatorname{Grad}(\dot{\overline{\mathbf{d}}}) \ge 0, \tag{11}$$

where the stress power is given in terms of the logarithmic strain rate $\dot{\eta}$ and its thermodynamically conjugate force α .

The rate of the Helmholtz free energy, Equation (10), is computed with respect to the rates of its arguments as

$$\dot{\psi} = \frac{\partial \psi}{\partial \boldsymbol{\eta}} : \dot{\boldsymbol{\eta}} + \frac{\partial \psi}{\partial \boldsymbol{D}} : \dot{\boldsymbol{D}} + \frac{\partial \psi}{\partial \xi_d} \dot{\xi}_d + \frac{\partial \psi}{\partial \mathbf{d}} \cdot \dot{\mathbf{d}} + \frac{\partial \psi}{\partial \operatorname{Grad}(\mathbf{d})} : \operatorname{Grad}(\dot{\mathbf{d}}). \tag{12}$$

Please note, that the partial derivative of the energy ψ with respect to the damage tensor \boldsymbol{D} yields the elastic, the additional damage hardening and the nonlocal damage driving forces \boldsymbol{Y}_e , \boldsymbol{Y}_h , and $\boldsymbol{Y}_{\overline{d}}$ that are defined as

$$\frac{\partial \psi}{\partial \mathbf{D}} = \underbrace{\frac{\partial \psi_e}{\partial \mathbf{D}}}_{=:-\mathbf{Y}_e} + \underbrace{\frac{\partial \psi_h}{\partial \mathbf{D}}}_{=:\mathbf{Y}_h} + \underbrace{\frac{\partial \psi_d^-}{\partial \mathbf{D}}}_{=:\mathbf{Y}_{\overline{I}}} =: -\mathbf{Y}. \tag{13}$$

In Section 3, we will present and compare the explicit forms of the nonlocal damage driving force $Y_{\overline{d}}$, since these differ for distinct choices of the micromorphic tuple, that is, the gradient-extension, whilst the other damage driving forces Y_e and Y_h remain unchanged.

0970207, 0, Downloaded from https://onlinelibrary.wiley.com/doi/10.1002/nme.7580 by Rwth Aachen Hochschulbibliothek, Wiley Online Library on [15/08/2024]. See the Terms and Conditional C

on Wiley Online Library for rules of use; OA articles are governed by the applicable Creative Commons License

Thereafter, the rates of Equation (12) are inserted into the balance equation, Equation (11), and yield by repositioning

$$\left(\alpha - \frac{\partial \psi}{\partial \boldsymbol{\eta}}\right) : \dot{\boldsymbol{\eta}} + (\underline{Y_e - Y_h - Y_{\overline{d}}}) : \dot{\boldsymbol{D}} + R_d \, \dot{\xi}_d
+ \left(\xi_{0_i} - \frac{\partial \psi}{\partial \overline{\mathbf{d}}}\right) \cdot \dot{\overline{\mathbf{d}}} + \left(\Xi_{0_i} - \frac{\partial \psi}{\partial \operatorname{Grad}(\overline{\mathbf{d}})}\right) : \operatorname{Grad}(\dot{\overline{\mathbf{d}}}) \ge 0.$$
(14)

State laws. The state laws are obtained by the Coleman and Noll⁶¹ procedure and the argumentation of Forest³⁹ as

$$\alpha = \frac{\partial \psi}{\partial \eta},\tag{15}$$

$$\xi_{0_i} = \frac{\partial \psi}{\partial \mathbf{d}},\tag{16}$$

$$\Xi_{0_{i}} = \frac{\partial \psi}{\partial \operatorname{Grad}(\overline{\mathbf{d}})},\tag{17}$$

and the reduced dissipation inequality with $R_d := -\partial \psi / \partial \xi_d$ as

$$\mathbf{Y}: \dot{\mathbf{D}} + R_d \ \dot{\xi}_d \ge 0. \tag{18}$$

Evolution equations. For the evolution of the internal variables D and ξ_d , we define two general convex, zero-valued, and non-negative inelastic potentials g_{d_1} and g_{d_2} in terms of the driving forces Y and R_d that yield the evolution equations

$$\dot{\mathbf{D}} = \dot{\gamma}_d \frac{\partial g_{d_1}}{\partial \mathbf{Y}},\tag{19}$$

$$\dot{\xi}_d = \dot{\gamma}_d \frac{\partial g_{d_2}}{\partial R_d},\tag{20}$$

where $\dot{\gamma}_d$ is the damage multiplier which is obtained by satisfying the damage onset criterion $\Phi_d(\mathbf{Y}, R_d) \leq 0$ in accordance with the Karush–Kuhn–Tucker conditions

$$\dot{\gamma}_d \ge 0, \quad \Phi_d \le 0, \quad \dot{\gamma}_d \Phi_d = 0.$$
 (21)

2.4 | Specific forms of Helmholtz free energy, damage onset criterion and inelastic potentials

Helmholtz free energy. Motivated by for example, Desmorat, ¹⁸ Badreddine et al., ¹⁷ Leukart and Ramm, ⁶ Lemaitre et al. ⁶² and similar to Simo, ⁶³ the elastic energy features a physically motivated split into isochoric and volumetric parts to account for the evolution of micro cracks and microvoids separately. Moreover, it fulfills the damage growth criterion ⁵⁸ and reads

$$\psi_e = \mu \operatorname{tr} \left(\operatorname{dev}(\boldsymbol{\eta})^2 (\boldsymbol{I} - \boldsymbol{D}) \right) \vartheta + f_d \mu \operatorname{tr} \left(\operatorname{dev}(\boldsymbol{\eta})^2 \right) (1 - \vartheta) + f_d \frac{K}{2} \operatorname{tr}(\boldsymbol{\eta})^2$$
(22)

with the isotropic degradation function

$$f_d = \left(1 - \frac{\operatorname{tr}(\mathbf{D})}{3}\right)^{e_d},\tag{23}$$

0970207, 0, Downloaded from https://onlinelibrary.wiley.com/doi/10.1002/nme.7580 by Rwth Aachen Hochschulbibliothek, Wiley Online Library on [15/08/2024]. See the Terms and Conditions

on Wiley Online Library for rules of use; OA articles are governed by the applicable Creative Commons License

where μ denotes the elastic shear modulus, κ the elastic bulk modulus, ϑ the degree of damage anisotropy, and e_d the exponent of the isotropic degradation function. Nonlinear and linear isotropic damage hardening are incorporated by

$$\psi_d = r_d \left(\xi_d + \frac{\exp(-s_d \, \xi_d) - 1}{s_d} \right) + \frac{1}{2} H_d \, \xi_d^2 \tag{24}$$

with the damage hardening parameters r_d , s_d and H_d . The additional kinematic damage hardening energy is formulated in terms of the eigenvalues D_i of the damage tensor

$$\psi_h = K_h \sum_{i=1}^{3} \left(-\frac{\left(1 - D_i\right)^{1 - \frac{1}{n_h}}}{1 - \frac{1}{n_h}} - D_i + \frac{1}{1 - \frac{1}{n_h}} \right), \tag{25}$$

where K_h and n_h are numerical parameters. The micromorphic energy contribution penalizes the difference between the components of the local and the nonlocal tuple by the numerical penalty parameters H_i and incorporates an internal length scale via the gradient of the nonlocal quantity and the materials parameters A_i for each component of the micromorphic tuple up to the total number of nonlocal degrees of freedom $n_{\overline{d}}$

$$\psi_{\overline{d}} = \frac{1}{2} \sum_{i=1}^{n_{\overline{d}}} H_i \left(d_i - \overline{d}_i \right)^2 + \frac{1}{2} \sum_{i=1}^{n_{\overline{d}}} A_i \operatorname{Grad} \left(\overline{d}_i \right) \cdot \operatorname{Grad} \left(\overline{d}_i \right). \tag{26}$$

Damage onset criterion. The chosen damage onset criterion with damage threshold Y_0

$$\Phi_d := \sqrt{3}\sqrt{Y_+ : \mathbb{A} : Y_+} - (Y_0 - R_d) \le 0 \tag{27}$$

features the option to include distortional damage hardening with the fourth order interaction tensor \mathbb{A} and material parameter c_d

$$\mathbb{A} = \left((\boldsymbol{I} - \boldsymbol{D})^{c_d} \otimes (\boldsymbol{I} - \boldsymbol{D})^{c_d} \right)^{\frac{23}{T}}$$
(28)

with the positive semi-definite part of the damage driving force being

$$Y_{+} = \sum_{i=1}^{3} \langle Y_{i} \rangle \boldsymbol{n}_{i}^{Y} \otimes \boldsymbol{n}_{i}^{Y}, \tag{29}$$

where $\langle \bullet \rangle = \max(\bullet, 0)$ and $\mathbf{n}_i^{\mathbf{Y}}$ denote the eigenvectors of the damage driving force \mathbf{Y} .

Inelastic potentials. The inelastic potential g_{d_1} for the evolution of the damage tensor is chosen in a pseudo-non-associative structure as

$$g_{d_1} = \frac{3}{2(Y_0 - R_d)} Y_+ : A : Y_+, \tag{30}$$

where the relation $\sqrt{3}\sqrt{Y_+}$: \mathbb{A} : $Y_+ = Y_0 - R_d$ obtained from Equation (27) for a converged state is utilized to avoid a division by zero in the local iteration (cf. Challamel et al.⁶⁴ and Holthusen et al.²³), when algorithmic differentiation (e.g., Korelc⁶⁵ and Korelc and Wriggers⁶⁶) is employed. However, the absolute value and direction of the evolution are identical to choosing an associative evolution equation, that is, $\dot{\mathbf{D}} = \partial \Phi_d / \partial \mathbf{Y}$. Furthermore, the inelastic potential g_{d_2} for the evolution of the accumulated damage is chosen linearly as

$$g_{d_{\lambda}} = R_d. \tag{31}$$

3 | MICROMORPHIC GRADIENT-EXTENSIONS

3.1 | Motivation

The novelty of this work lies in the comparison of different gradient-extensions for anisotropic damage with respect to their efficiency and accuracy. To ensure the comparability of the results, the same local anisotropic damage formulation is utilized throughout this work and only the choice of the local micromorphic tuple, that is, the selection of local quantities whose localization is prevented by the gradient-extensions, is adapted. Here, we restrict ourselves to invariant-based micromorphic tuples of the damage tensor and are, thus, able to study the effect of different nonlocal damage driving forces.

Other authors, for example, Fassin et al., ¹⁹ Fassin et al., ²⁰ and Sprave and Menzel, ¹⁴ investigated the regularization of a scalar damage hardening variable. However, as pointed out by Fassin et al., ²⁰ this procedure can violate the differentiability of the damage onset function when employing associative damage evolution by maximizing the dissipation and is, thus, not considered in this context.

In the following, we present three model formulations (models A, B, and C) with full, using six nonlocal degrees of freedom, and reduced regularization of the damage tensor, using three and two nonlocal degrees of freedom.

Full regularization. Initially, we strive for a rigorous regularization, that is, a regularization of all independent components, of the damage tensor and, therefore, in model A, all six independent components of the symmetric second order damage tensor are regularized individually. Thereby, no mesh dependence of any component of the damage tensor is expected to occur and, furthermore, an accurate reference solution for the reduced regularizations is obtained. A similar procedure can be found in Langenfeld and Mosler, where the six independent components of the integrity tensor are regularized. However, a full regularization requires six additional nonlocal micromorphic degrees of freedom and, thus, triples the number of global degrees of freedom compared to the local, purely mechanical problem. Due to this significant increase in degrees of freedom, we aim to reduce the former and to simultaneously maintain the regularization's accuracy.

Reduced principal traces regularization. The idea for the first reduced regularization is based on the uniqueness of the eigenvalues of the damage tensor. A regularization of the former should, thus, also lead to a proper regularization of the entire tensor. For the ease of numerical implementation and since the principal traces of the damage tensor can unambiguously determined from its eigenvalues, model B utilizes the reduced micromorphic tuple of Holthusen et al.²³ In this formulation, the micromorphic tuple contains the three principal traces of the damage tensor to each of which a corresponding nonlocal counterpart is introduced. Compared to model A, model B requires three nonlocal degrees of freedom less, but still doubles the total number of degrees of freedom compared to the local model.

Reduced volumetric-deviatoric regularization. We, therefore, aim to achieve a further reduction in the required number of nonlocal degrees of freedom and motivate a regularization of the volumetric and deviatoric part of the damage tensor based on two nonlocal degrees of freedom. Since isotropic damage yields by its nature and the sole consideration of microvoids a volumetric damage tensor *DI* and requires only a single nonlocal degree of freedom, we aim to capture the damage anisotropy due to the micro cracks by a regularization of the deviatoric part of the damage tensor as is has been suggested for investigation in Holthusen et al.⁶⁷ A further advantage of model C becomes apparent when considering isotropic damage, since only one nonlocal degree of freedom is non-zero whereas for model A and B still three nonlocal degrees of freedom are non-zero.

3.2 | Specific micromorphic tuples

To ensure all models' objectivity, the micromorphic tuples are formulated based on invariants of the damage tensor. For the micromorphic tuple of model A, we introduce six general structural tensors M_1 , M_2 , M_3 , M_4 , M_5 , and M_6 that yield

$$\mathbf{d}^{\mathbf{A}} = (\operatorname{tr}(\mathbf{D}\mathbf{M}_{1}), \operatorname{tr}(\mathbf{D}\mathbf{M}_{2}), \operatorname{tr}(\mathbf{D}\mathbf{M}_{3}), \operatorname{tr}(\mathbf{D}\mathbf{M}_{4}), \operatorname{tr}(\mathbf{D}\mathbf{M}_{5}), \operatorname{tr}(\mathbf{D}\mathbf{M}_{6})). \tag{32}$$

.0970207, 0, Downloaded from https://onlinelibrary.wiley.com/doi/10.1002/nme.7580 by Rwth Aachen Hochschulbibliothek, Wiley Online Library on [15/08/2024]. See the Terms and Conditions

Here, the term structural tensor is employed generically for the invariant-based tuple definition and does not refer to microstructural material characteristics. In order to control the normal and shear components of the damage tensor, we specify the structural tensors according to the Cartesian basis vectors e_1 , e_2 , and e_3 as

$$M_1 = \mathbf{e}_1 \otimes \mathbf{e}_1, M_2 = \mathbf{e}_2 \otimes \mathbf{e}_2, M_3 = \mathbf{e}_3 \otimes \mathbf{e}_3,$$

$$M_4 = \mathbf{e}_1 \otimes \mathbf{e}_2, M_5 = \mathbf{e}_1 \otimes \mathbf{e}_3, M_6 = \mathbf{e}_2 \otimes \mathbf{e}_3.$$
(33)

The micromorphic tuple based on the principal traces of the damage tensor of model B stems from Holthusen et al.²³ and reads

$$\mathbf{d}^{\mathrm{B}} = (\operatorname{tr}(\mathbf{D}), \operatorname{tr}(\mathbf{D}^{2}), \operatorname{tr}(\mathbf{D}^{3})). \tag{34}$$

Finally, the micromorphic tuple of model C with a split of the damage tensor into volumetric and deviatoric part reads

$$\mathbf{d}^{C} = \left(\frac{\operatorname{tr}(\mathbf{D})}{3}, \operatorname{tr}\left(\operatorname{dev}(\mathbf{D})^{2}\right)\right). \tag{35}$$

3.3 | Explicit nonlocal damage driving forces

Next, we compare the explicit forms of the nonlocal damage driving forces that are derived from $Y_{\overline{d}} = \partial \psi_{\overline{d}} / \partial D$. Their general form depends on the number of elements per micromorphic tuple $n_{\overline{d}}$ and reads

$$Y_{\overline{d}} = \sum_{i=1}^{n_{\overline{d}}} H_i \left(d_i - \overline{d}_i \right) \frac{\partial d_i}{\partial \mathbf{D}}.$$
 (36)

The explicit form of the nonlocal damage driving force of model A reads under the consideration of the symmetry of D

$$Y_{\overline{d}}^{A} = H_{1}\left(\operatorname{tr}\left(\boldsymbol{D}\boldsymbol{M}_{1}\right) - \overline{d}_{1}\right)\operatorname{sym}(\boldsymbol{M}_{1})$$

$$+ H_{2}\left(\operatorname{tr}\left(\boldsymbol{D}\boldsymbol{M}_{2}\right) - \overline{d}_{2}\right)\operatorname{sym}(\boldsymbol{M}_{2})$$

$$+ H_{3}\left(\operatorname{tr}\left(\boldsymbol{D}\boldsymbol{M}_{3}\right) - \overline{d}_{3}\right)\operatorname{sym}(\boldsymbol{M}_{3})$$

$$+ H_{4}\left(\operatorname{tr}\left(\boldsymbol{D}\boldsymbol{M}_{4}\right) - \overline{d}_{4}\right)\operatorname{sym}(\boldsymbol{M}_{4})$$

$$+ H_{5}\left(\operatorname{tr}\left(\boldsymbol{D}\boldsymbol{M}_{5}\right) - \overline{d}_{5}\right)\operatorname{sym}(\boldsymbol{M}_{5})$$

$$+ H_{6}\left(\operatorname{tr}\left(\boldsymbol{D}\boldsymbol{M}_{6}\right) - \overline{d}_{6}\right)\operatorname{sym}(\boldsymbol{M}_{6}).$$
(37)

With $\partial \operatorname{tr}(\mathbf{D}^i)/\partial \mathbf{D} = i \mathbf{D}^{i-1}$, the explicit form for model B reads

$$\mathbf{Y}_{\overline{d}}^{B} = H_{1} \left(\operatorname{tr} \left(\mathbf{D} \right) - \overline{d}_{1} \right) \mathbf{I}$$

$$+ H_{2} \left(\operatorname{tr} \left(\mathbf{D}^{2} \right) - \overline{d}_{2} \right) 2 \mathbf{D}$$

$$+ H_{3} \left(\operatorname{tr} \left(\mathbf{D}^{3} \right) - \overline{d}_{3} \right) 3 \mathbf{D}^{2}.$$
(38)

And using $dev(\mathbf{D}) = \mathbf{D} - tr(\mathbf{D})/3 \mathbf{I}$, the explicit form for model C reads

$$\mathbf{Y}_{\overline{d}}^{C} = \frac{H_{1}}{3} \left(\frac{\operatorname{tr}(\mathbf{D})}{3} - \overline{d}_{1} \right) \mathbf{I}
+ H_{2} \left(\operatorname{tr} \left(\operatorname{dev}(\mathbf{D})^{2} \right) - \overline{d}_{2} \right) \left(2\mathbf{D} - \frac{2}{3} \operatorname{tr}(\mathbf{D}) \mathbf{I} \right).$$
(39)

When comparing the damage driving forces of model A, B, and C, Equations (37)–(39), their different structures are evident and, thus, also for identical choices of the parameters $H_1, \ldots, H_{n_{\overline{d}}}$ and $A_1, \ldots, A_{n_{\overline{d}}}$ different model responses are to be expected.

4 | NUMERICAL EXAMPLES

The aim of this section is to study the interesting research question whether an accurate regularization of anisotropic damage models can efficiently be obtained by a reduced regularization of the damage tensor. Therefore, we investigate four representative structural examples by utilizing models A, B, and C and are, thus, able to identify the effect of the gradient-extension with the simulation of the very same boundary value problem with different models. Further, we can directly compare the accuracy of the reduced regularizations (models B and C) to the reference solution with full regularization (model A).

The material point behavior of the anisotropic damage model was examined in detail in Holthusen et al.²³ to which we kindly refer the interested reader for further information. The generic material parameters are, unless stated otherwise, adopted from Brepols et al.⁶⁸ and Holthusen et al.²³ and listed in Table 1. For each example, the internal length scales A_i of models A and C were identified such that the maximum force of the structural response coincided with the one obtained by model B. For the examples in Sections 4.1,4.3, and 4.4, the internal length scales of model B were chosen in line with Holthusen et al.⁶⁷ as $A_i^B = 75$ [MPa mm²] and for the example in Section 4.2 in line with Holthusen et al.²³ as $A_i^B = 100$ [MPa mm²]. The Taylor series sampling point a_h listed in Table 1 is required for the implementation of the kinematic damage driving force (cf. Holthusen et al.²³), but was omitted in the model presentation in Section 2. In order to avoid snap-backs during the simulation, an artificial viscosity η_{ν} is utilized. Comprehensive studies in Sections 4.1 and 4.2 confirm that the results are unaffected by the artificial viscosity for a choice of $\eta_{\nu} = 1$ [MPa s]. The two-dimensional examples in Sections 4.1,4.2 and 4.4 utilize four-node quadrilateral plane-strain elements and the three-dimensional example in Section 4.3 utilizes eight-node hexahedral elements. In all simulations, linear shape functions are employed for the displacement and micromorphic degrees of freedom.

TABLE 1 Material and numerical parameters.

Symbol	Material parameter	Value	Unit
μ	Elastic shear modulus	55,000	MPa
K	Elastic bulk modulus	61666.6	MPa
θ	Damage anisotropy	0/1	-
e_d	Isotropic degradation function exponent	1	-
Y_0	Initial damage threshold	2.5	MPa
c_d	Distortional hardening exponent	1	-
H_d	Linear isotropic hardening prefactor	1	MPa
r_d	Nonlinear isotropic hardening prefactor	5	MPa
s_d	Nonlinear isotropic hardening scaling factor	100	-
K_h	Kinematic hardening prefactor	0.1	MPa
n_h	Kinematic hardening exponent	2	-
A_i	Internal length scales	75–1300	MPa mm²
Symbol	Numerical parameter	Value	Unit
a_h	Taylor series sampling point	0.999999	-
H_i	Micromorphic penalty parameters	10^{4}	MPa
$\eta_{\scriptscriptstyle \mathcal{V}}$	Artificial viscosity	1	MPa s

The finite element simulations were conducted using the software *FEAP*, ⁶⁹ new finite element meshes for the example of Section 4.4 were created with the software *HyperMesh*, ⁷⁰ and post-processing of the simulations' results was carried out with *ParaView*. ⁷¹

4.1 | Plate with hole specimen

The first example is characterized by a tension dominated loading situation and considers a plate with hole specimen. This example was, in the context of isotropic damage, previously investigated by for example, Friedlein et al., ⁷² Sprave and Menzel, ⁷³ Kiefer et al., ⁷⁴ Brepols et al., ⁷⁵ and Dimitrijevic and Hackl ³⁶ and, for anisotropic damage, by for example, Sprave and Menzel, ¹⁴ Langenfeld and Mosler, ¹³ and Fassin et al. ²⁰

Figure 1 shows the geometry and the considered boundary value problem. The dimensions read $l=100~\mathrm{[mm]}$ and $r=50~\mathrm{[mm]}$ with a thickness of 1 [mm]. Due to symmetry, only one quarter of the specimen is modeled in the simulation and the top edge is moved in vertical direction by a prescribed displacement. The two-dimensional finite element meshes stem from Fassin et al.²⁰ and the mesh with 2039 elements contains 2141 nodes, the mesh with 2651 elements contains 2784 nodes, the mesh with 5302 elements contains 5484 nodes, and the mesh with 14,752 elements contains 15,033 nodes. The internal length scales of model B are chosen as $A_i^{\mathrm{B}}=75~\mathrm{[MPa~mm^2]}$ and the parameters of model A and C are identified as $A_i^{\mathrm{A}}=420~\mathrm{[MPa~mm^2]}$ and $A_i^{\mathrm{C}}=1300~\mathrm{[MPa~mm^2]}$.

In Figure 2, the normalized force-displacement curves prove mesh convergence for all models already upon the first refinement with 2651 elements (see Figure 2A-C). Furthermore, Figure 2D provides the direct comparison of all models using the finest mesh with 14,752 elements. Model A and C yield an identical structural response, while the vertical force drop of model B is shifted to the right with $u_{0.5\ F_{\text{max}}}^{\text{B}} = 0.751\ [\text{mm}]$ compared to $u_{0.5\ F}^{\text{A,C}} = 0.706\ [\text{mm}]$.

 $u_{0.5\,F_{\rm max}}^{\rm A,C}=0.706$ [mm].

Figure 3 shows the damage contour plots at the end of the simulation. For all models, the width of the damage zone of component D_{yy} is thicker than that of component D_{xx} , since the specimen is loaded in y-direction. Models A and C yield coinciding results, whilst for model B, the damage zone for both normal components of the damage tensor are more pronounced. This observation is consistent with the results of Figure 2D, where, loosely speaking, the area under the force-displacement curve is larger for model B and, hence, a larger amount of energy is dissipated in this case, which implies that the corresponding damage zones have to be larger as well.

The Green-Lagrange strain components at the end of the simulation are presented in Figure 4. The maximum strain in loading direction yields for model A a value of $E_{yy}^{A} = 6.452$ [-], for model B a value of $E_{yy}^{B} = 8.287$ [-], and for model C

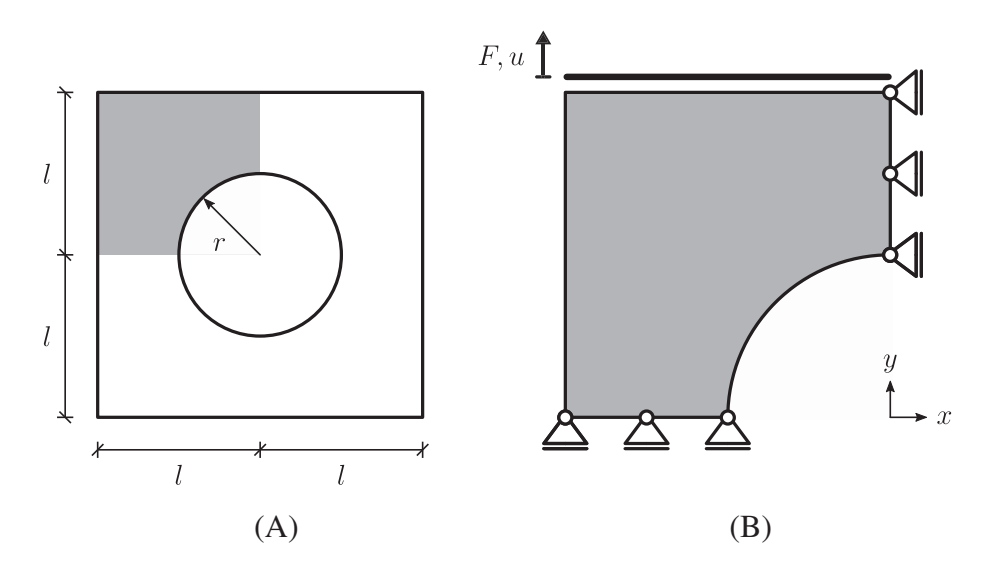


FIGURE 1 Geometry and boundary value problem of the plate with hole specimen. (A) Geometry. (B) Boundary value problem.

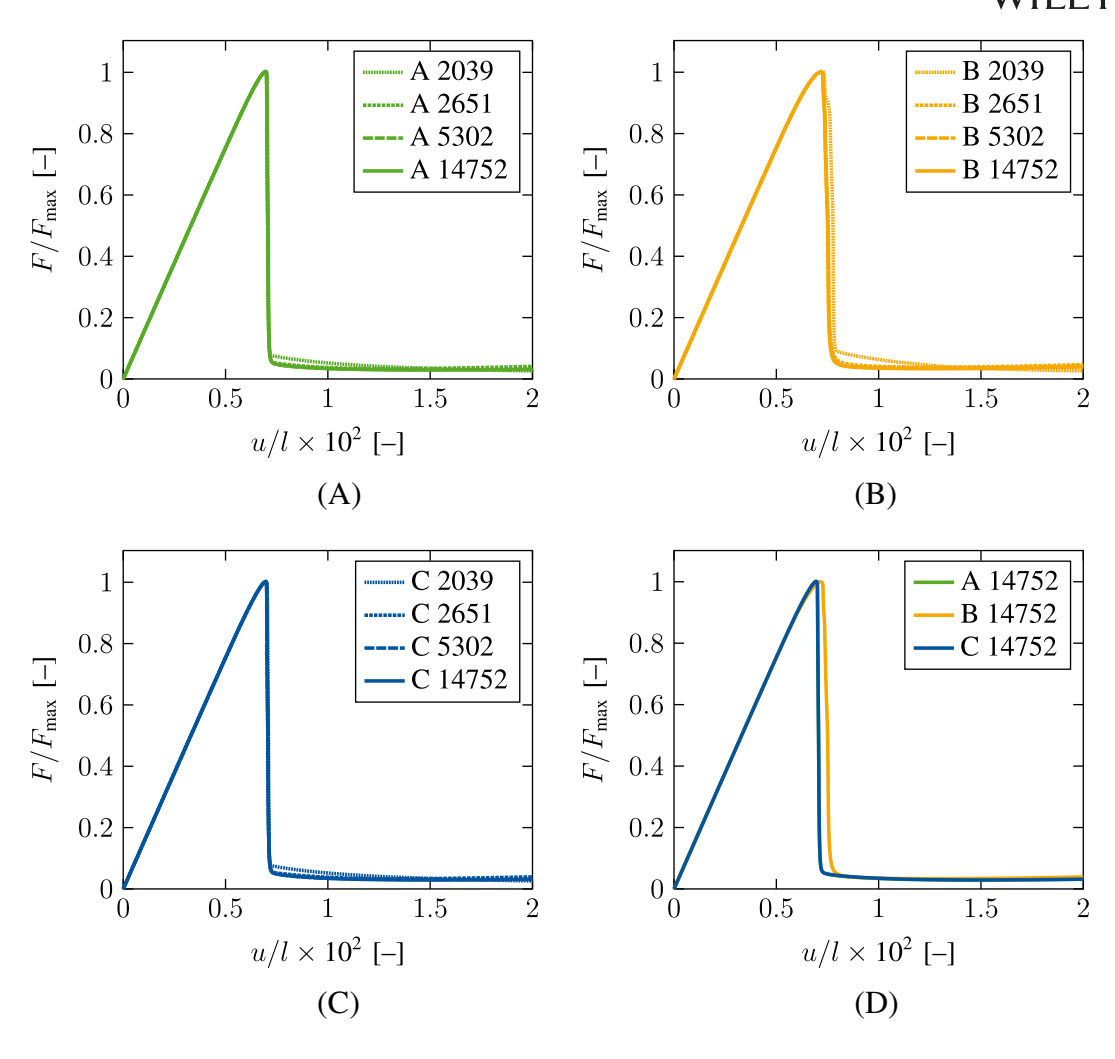


FIGURE 2 Mesh convergence studies for the plate with hole specimen and model comparison. The forces are normalized with respect to the maximum force of the finest mesh (14,752 elements) of model B with $F_{\text{max}} = 5.0767 \times 10^4$ [N]. (A) Model A. (B) Model B. (C) Model C. (D) Model comparison.

a value of $E_{yy}^{C} = 5.747$ [-]. The deformed shapes of the specimen and the strain distributions conform for model A and model C while model B exhibits stronger necking at the inner edges.

Next, we examine the necessity of using an anisotropic damage formulation, here that is, $\vartheta=1$ [-], compared to an isotropic one, that is, $\vartheta=0$ [-]. Figure 5 shows the force-displacement curves of the plate with hole simulation with the finest mesh (14,752 elements) for all models using the anisotropic and isotropic model formulation. The isotropic damage formulations overestimate the structure's maximum load bearing capacity (A: +4.18 [%], B: +4.26 [%], C: +4.58 [%]). Hence, the identification of material parameters based on experimental data requires the user to consider the differences between isotropic and anisotropic damage models and to design the experiments accordingly. Deviations in the resulting damage contour plots for anisotropic and isotropic damage can also be observed in Figure 6, where the shape and intensity are clearly nonconforming at the edges of the damage zone.

Then, we investigate the behavior of the local model formulation without utilizing a gradient-extension, analogously to Fassin et al.,²⁰ in order to ensure that no regularizing effects result from the use of an artificial viscosity. Figure 7 shows the force-displacement curves for different mesh-discretizations and, as clearly indicated by the enlarged image section, no convergence with respect to the maximum force can be observed upon mesh refinement. This observation suggests the occurrence of localization in the simulation, which is confirmed by the damage contour plots in Figure 8, where the crack localizes into a single row of elements for each mesh. From the results of

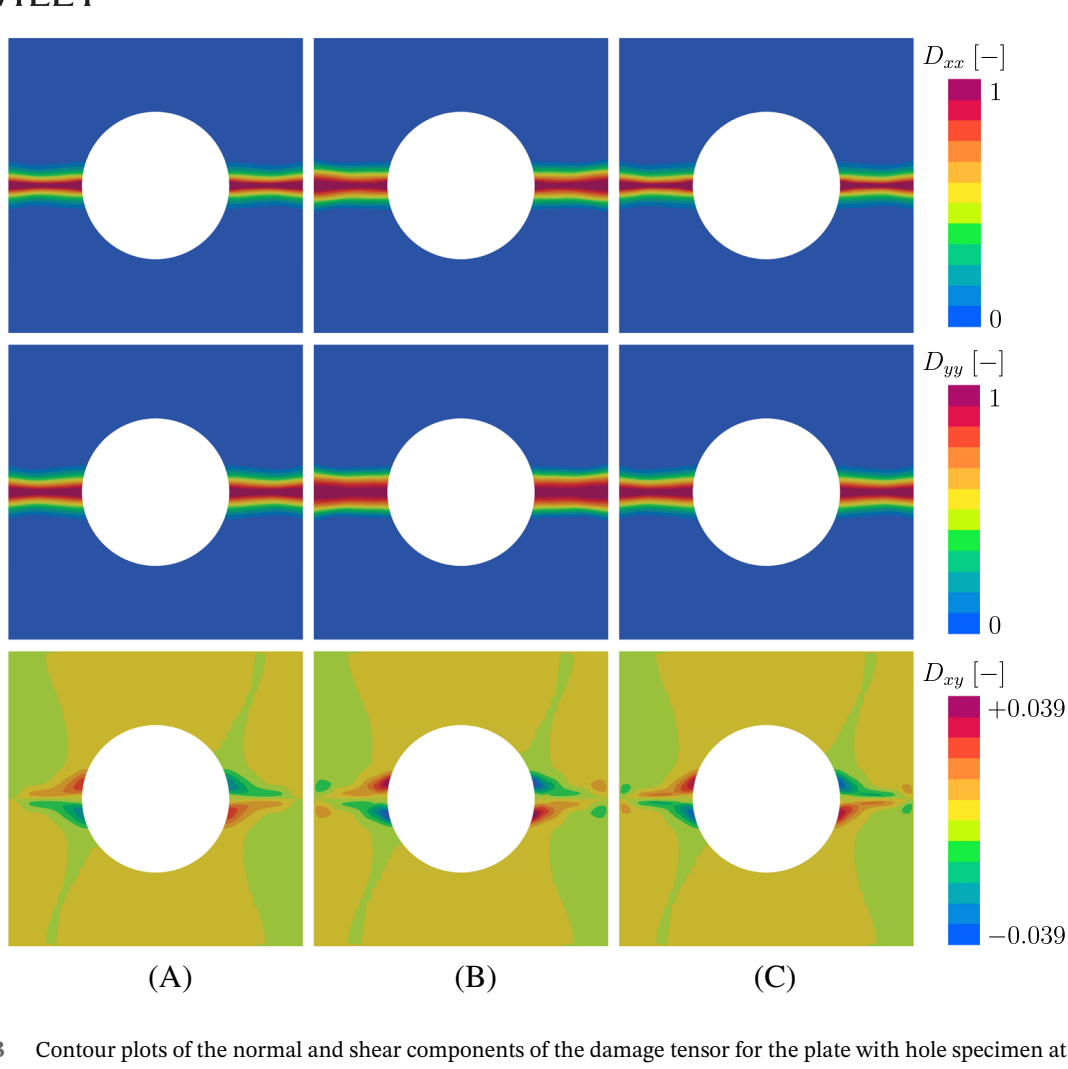


FIGURE 3 Contour plots of the normal and shear components of the damage tensor for the plate with hole specimen at the end of the simulation. (A) Model A. (B) Model B. (C) Model C.

Figures 7 and 8 we can infer that the consideration of a sufficiently small artificial viscosity, here $\eta_{\nu} = 1$ [N s/mm²], does not cure the mesh dependence of the local damage model and, thus, does not interfere with the investigated regularizations.

Nevertheless, the model's response is obviously not completely independent of the choice of the artificial viscosity. Thus, we study the influence of the parameter η_{ν} in Figures 9 and 10 using model C. Figure 9 shows the increasing the artificial viscosity leads to a less step drop in the force-displacement curve after reaching the maximum peak load and, also, to a higher residual force after the failure of the specimen. However, the maximum load bearing capacity of the structure is unaffected by a variation of η_{ν} . Figure 10 shows the difference plots for the components of the damage tensor comparing the results of using $\eta_{\nu} = 1$ [N s/mm²] versus $\eta_{\nu} = 2/4/10$ [N s/mm²]. Even for an increase of the artificial viscosity by a factor of ten, the maximum difference for the normal and shear components yields only values of $|\Delta D_{xx}| = 0.0386$ [–], $|\Delta D_{yy}| = 0.0395$ [–], and $|\Delta D_{xy}| = 0.0015$ [–].

These studies have proven the negligible influence of the artificial viscosity on the results of the simulation and justify its use in the present work to allow for a displacement-driven load control.

For model C, the evolution of the components of the micromorphic tuple and their differences to their local counterparts are presented in Figure 11 for the states of crack initiation, crack propagation and failure. Inside and in the vicinity of the crack, the nonlocal variable \overline{d}_1 that is associated with $\operatorname{tr}(\mathbf{D})/3$ evolves towards a value of one and the nonlocal variable \overline{d}_2 that is associated with $\operatorname{tr}(\operatorname{dev}(\mathbf{D})^2)$ initially grows, but eventually evolves towards a value of zero. The differences of the micromorphic tuple's components and the local tuple's components is restricted to $(\overline{d}_1 - d_1)[-] \in [-0.0343, 0.0149]$

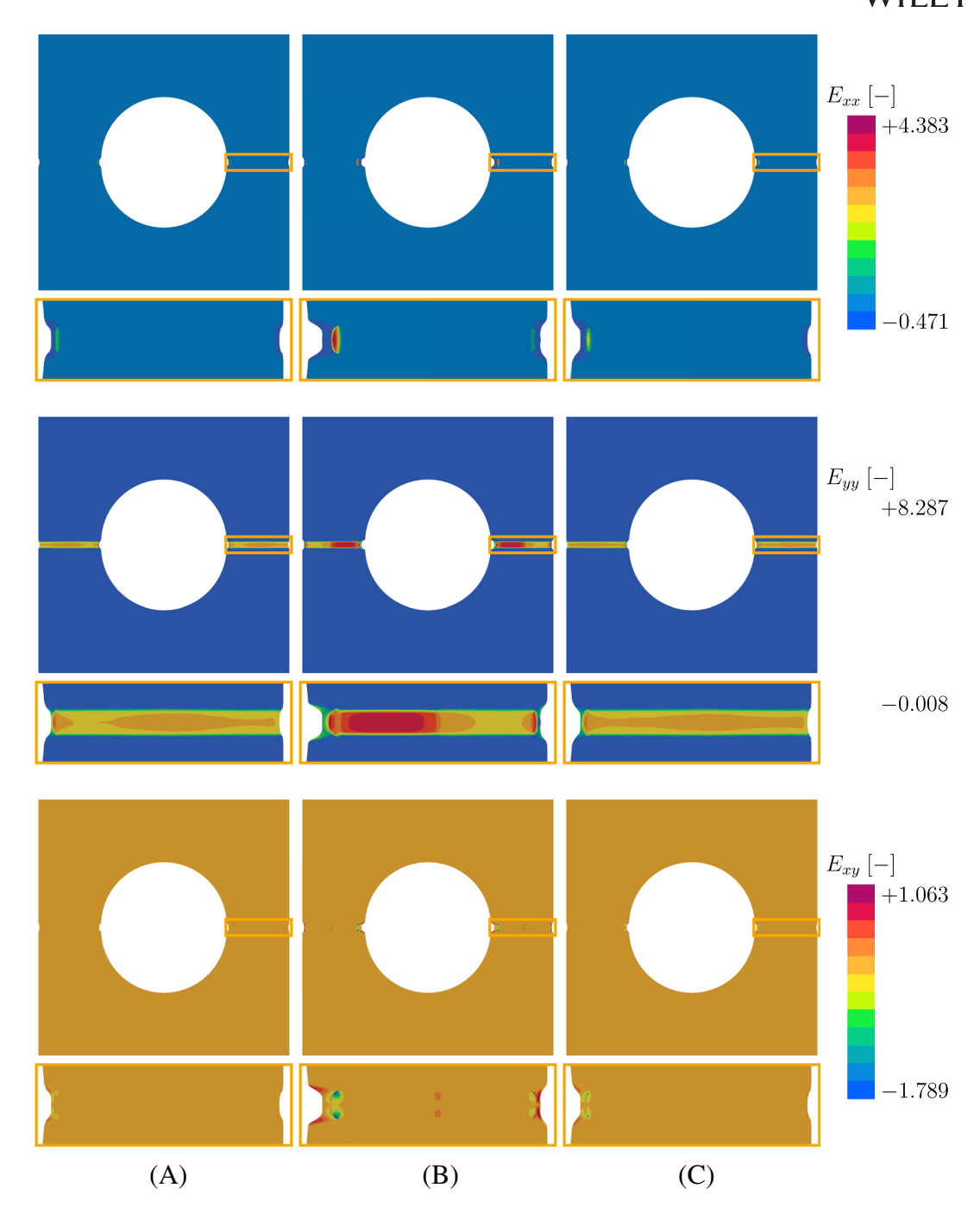


FIGURE 4 Contour plots of the normal and shear components of the Green-Lagrange strain tensor for the plate with hole specimen at the end of the simulation on the deformed configuration. (A) Model A. (B) Model B. (C) Model C.

and $(\overline{d}_2 - d_2)[-] \in [-0.0164, 0.0160]$. Thus, the choice of the micromorphic penalty parameter $H_i = 10^4$ [MPa] ensures a consistent evolution of the micromorphic and the local tuple.

4.2 | Asymmetrically notched specimen

The next example compares the three gradient-extensions for a combined tension and shear loading situation and considers an asymmetrically notched specimen. This example has also been investigated in for example, Friedlein et al.,⁴

FIGURE 5 Comparison of the force-displacement curves of the anisotropic and isotropic computation for the plate with hole specimen (14,752 elements). The forces are normalized with respect to the maximum force of the anisotropic computation of model B with $F_{\text{max}} = 5.0767 \times 10^4 \text{ [N]}.$

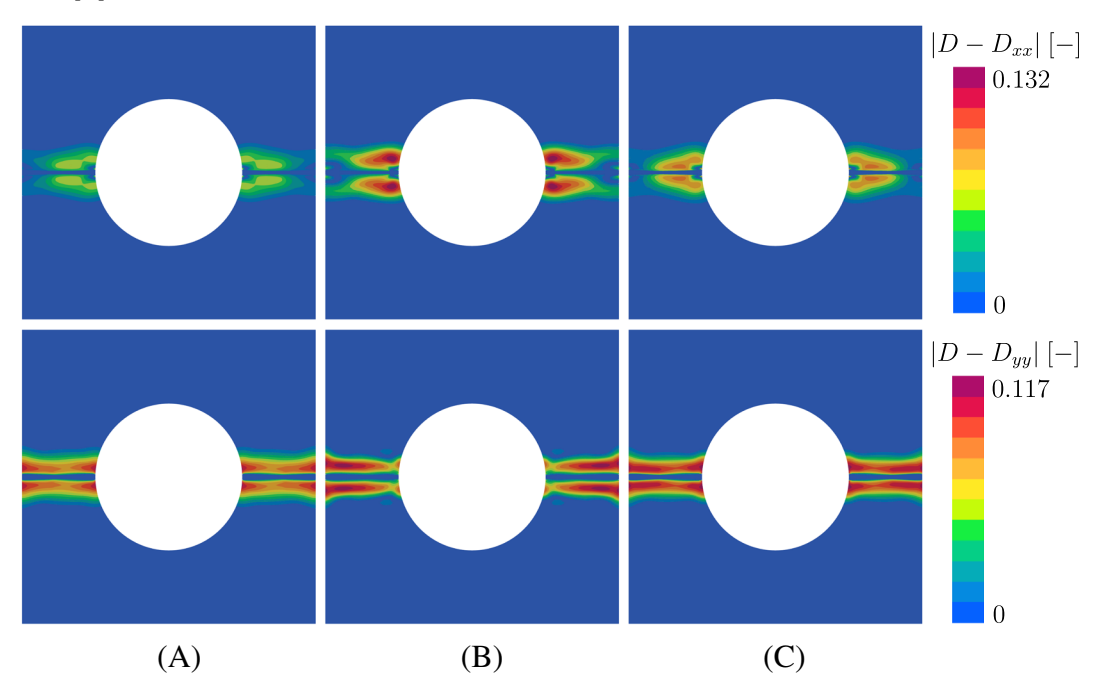


FIGURE 6 Comparison of the damage contour plots of the anisotropic and isotropic computation for the plate with hole specimen by a difference plot of the isotropic damage value D compared to the normal components of the anisotropic damage tensor D_{xx} and D_{yy} . (A) Model A. (B) Model B. (C) Model C.

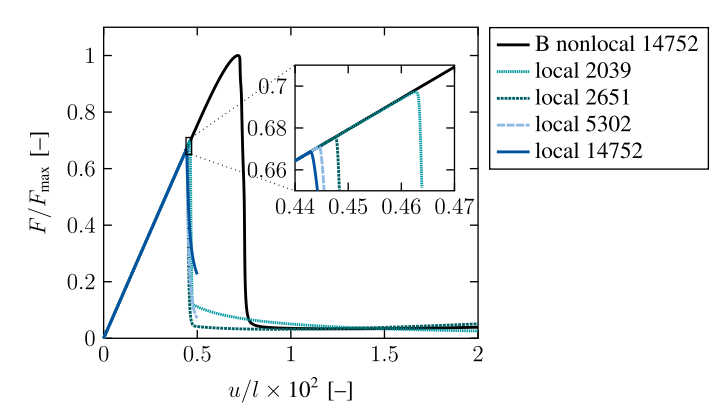


FIGURE 7 Force-displacement curves for the local damage model without gradient-extension for the plate with hole specimen for increasing degrees of mesh refinement. The forces are normalized with respect to the maximum force of the nonlocal computation of model B with $F_{\text{max}} = 5.0767 \times 10^4$ [N].

FIGURE 8 Damage contour plots for the local anisotropic damage model for the plate with hole specimen captured at position $u/l \times 10^2 = 0.5$ [-] from Figure 7 for different mesh discretizations. The damage values are averaged over all Gauss-points per element. (A) 2039. (B) 2651. (C) 5302. (D) 14,752.

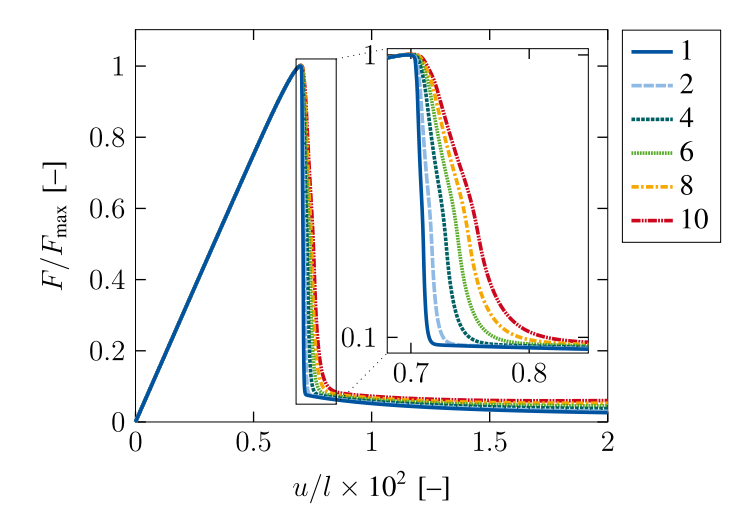


FIGURE 9 Force-displacement curves for the plate with hole specimen using model C for a variation of the artificial viscosity η_{ν} (mesh 2039). The forces are normalized with respect to the maximum force of $\eta_{\nu} = 1$ [N s/mm²] (2039 elements) with $F_{\text{max}} = 5.0920 \times 10^4$ [N].

Felder et al.,⁷⁶ Barfusz et al.,⁷⁷ Brepols et al.,⁶⁸ Ambati et al.⁷⁸ and also in Holthusen et al.,²³ where the same boundary value problem with the same material parameters is solved for model B using an arc-length controlled method yielding a double snap-back. These results serve in this section as an additional reference solution for model B and confirm the displacement controlled simulation results using the artificial viscosity.

Figure 12 shows the geometry and the corresponding boundary value problem. The dimensions read h=36 [mm], l=100 [mm], l=10

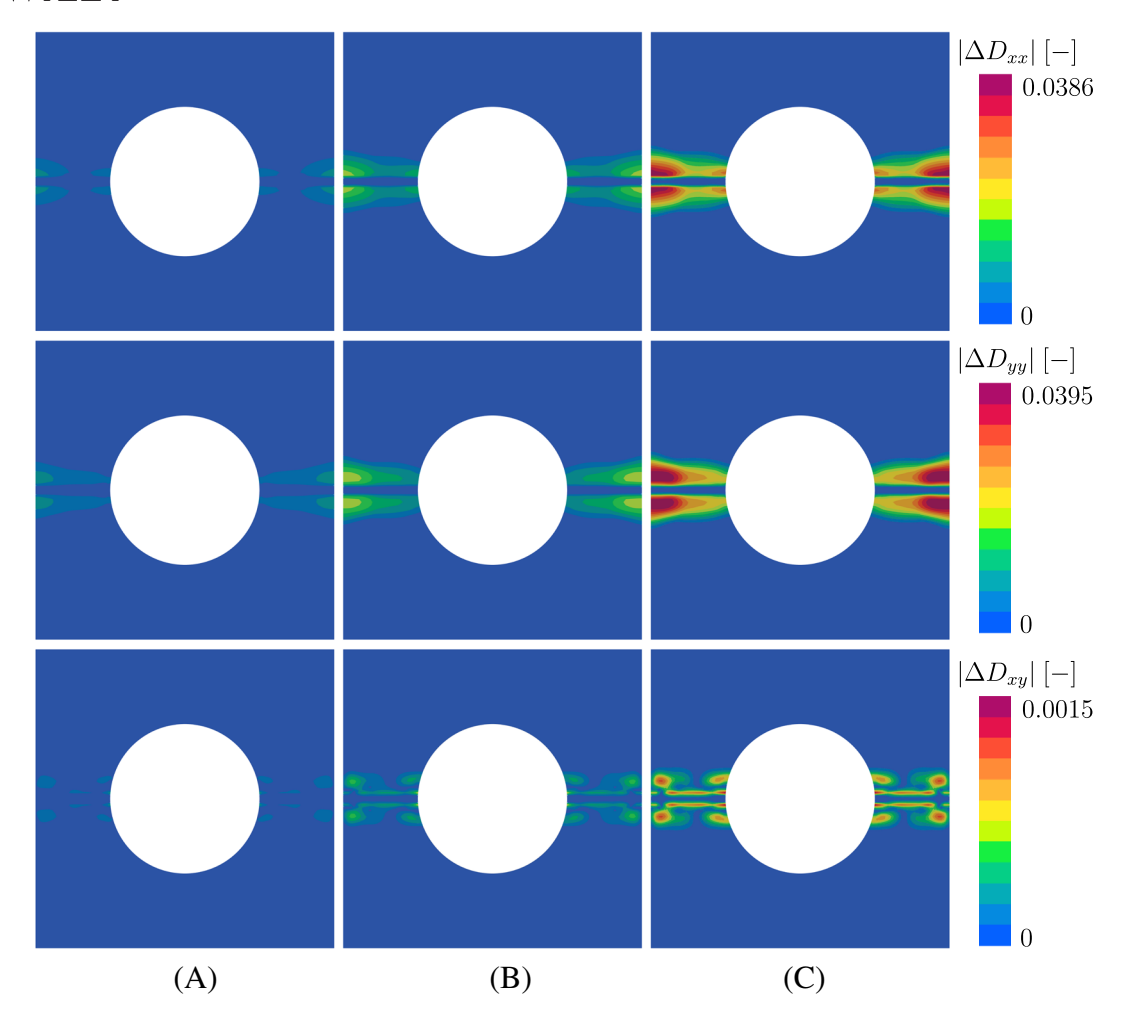


FIGURE 10 Difference plot of the damage contours of the normal and shear components of the damage tensor for the plate with hole specimen using model C for different values of the artificial viscosity η_v at the end of the simulation of Figure 9. (A) $\eta_v = 1$ vs. 2 [N s/mm²]. (B) $\eta_v = 1$ vs. 4 [N s/mm²]. (C) $\eta_v = 1$ vs. 10 [N s/mm²].

Figure 13 shows the normalized force-displacement curves for the asymmetrically notched specimen and all models predict the maximum peak force also with the coarsest mesh (1624 elements) accurately. In the post-failure regime, models A and C show with increasing mesh refinement less deviations from the final solution compared to model B (see Figure 13A–C). The model comparison in Figure 13D shows that, analogously to the tension dominated example in Section 4.1, the vertical drop of model B is shifted to the right, that is, $u_{0.5\ F_{\rm max}}^{\rm B} = 1.062\ [{\rm mm}]$ compared to $u_{0.5\ F_{\rm max}}^{\rm A} = 0.947\ [{\rm mm}]$ and $u_{0.5\ F_{\rm max}}^{\rm C} = 0.955\ [{\rm mm}]$.

In Figure 14, the damage contour plots with a zoom to the center of the asymmetrically notched specimen are presented. All models demonstrate the formation of a shear crack between the notches as well as a more pronounced evolution of the damage component D_{xx} , since the x-direction corresponds to the loading direction. With regard to the normal components of the damage tensor, the results of models A and C differ in shape and intensity compared to model B. While models A and C yield a sigmoidal crack pattern, model B yields a straight shear crack. Moreover, the total width of the damage zone for model B is greater than for models A and C, which is in line with the findings of Section 4.1. When comparing the shear components of the damage tensor, model A yields the evolution of D_{xy} over a wider spread area compared to models B and C, but exhibits no distinct peak values at the notches. The smoothed out distribution of D_{xy} can result from the strict regularization properties of model A that controls each component of the damage tensor individually.

The study comparing isotropic and anisotropic damage for the asymmetrically notched specimen is presented in Figure 15. The force-displacement curves yield also for this example a significant overestimation of the maximum peak

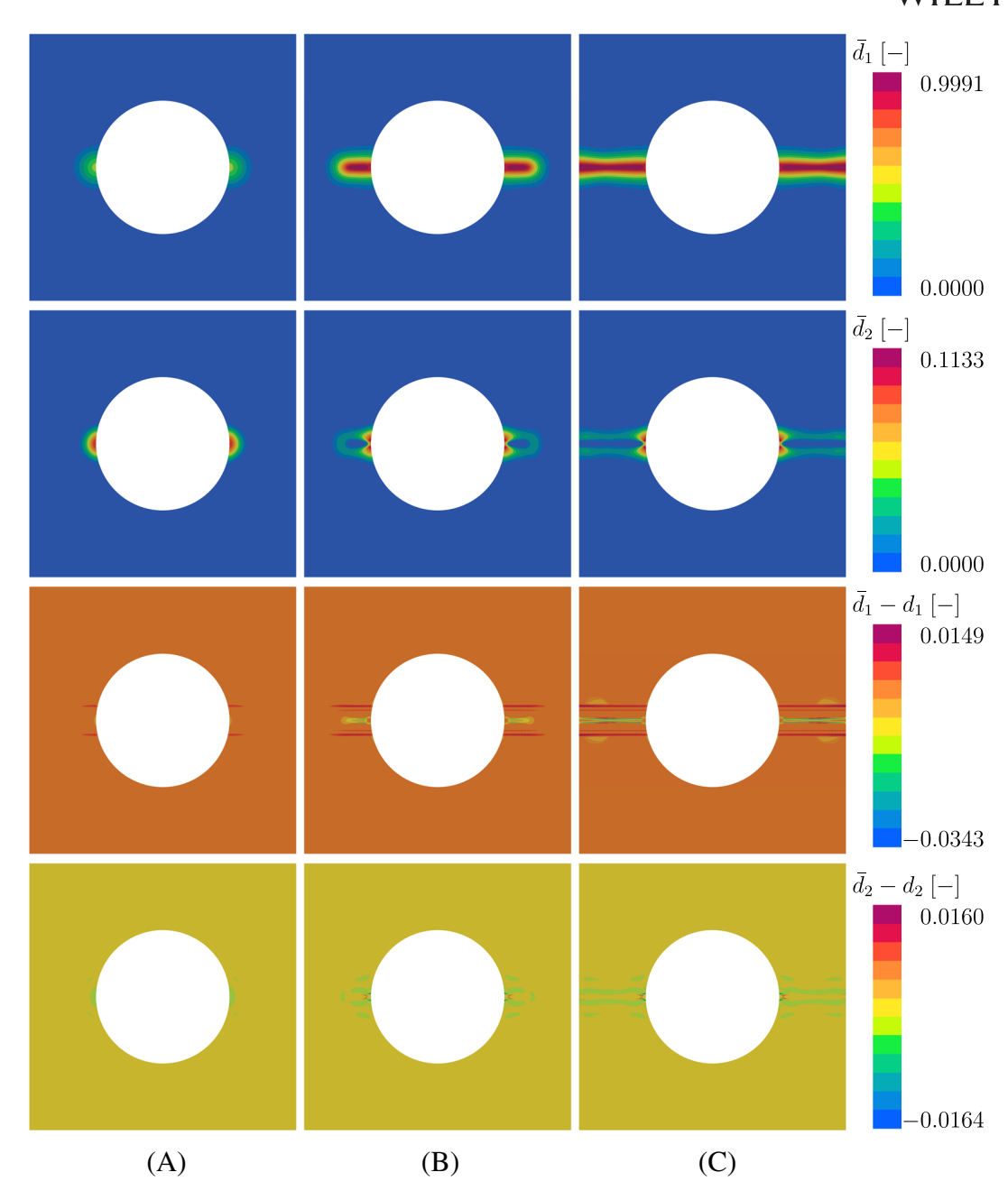


FIGURE 11 Contour plots for the evolution of the micromorphic degrees of freedom and their differences to the components of the local micromorphic tuple for the plate with hole specimen using model C. (A) Initiation. (B) Propagation. (C) Failure.

force when considering only an isotropic damage formulation (A: +4.86 [%], B: +6.00 [%], C: +6.03 [%]) and corroborates that damage has to be modeled as an anisotropic phenomenon.

Finally, this example serves to compare the displacement driven load control using artificial viscosity to an arc-length driven load control without artificial viscosity for model B. Figure 16 shows the force-displacement curves for both load control procedures, where the arc-length controlled reference solution is obtained from Holthusen et al.²³ Both procedures yield the same maximum peak force also for coarse meshes. Then, the displacement driven procedure yields a vertical drop of the force-displacement curve while the arc-length controlled procedure yields a double snap-back during the force decrease. Thereafter, the curves again unite and are congruent with each other and, thus, proof that both control procedures, with and without artificial viscosity, are equally valid.

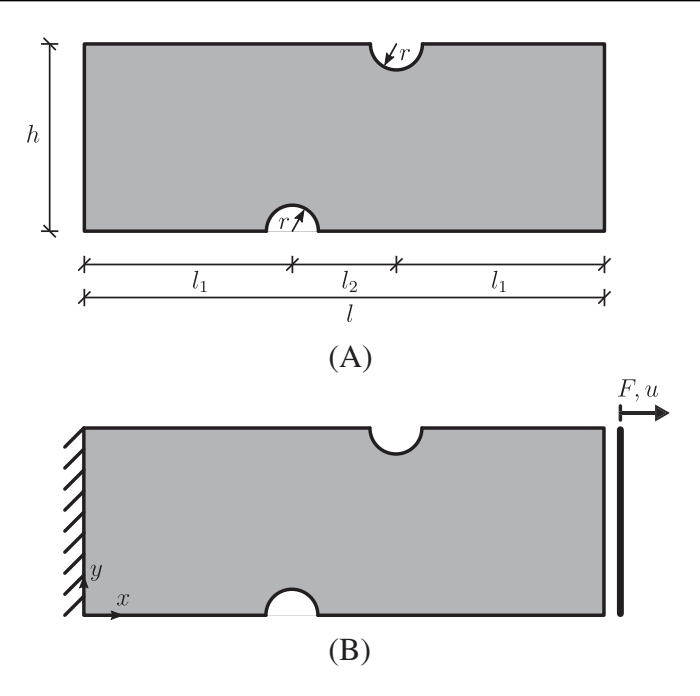


FIGURE 12 (A) Geometry and (B) boundary value problem of the asymmetrically notched specimen.

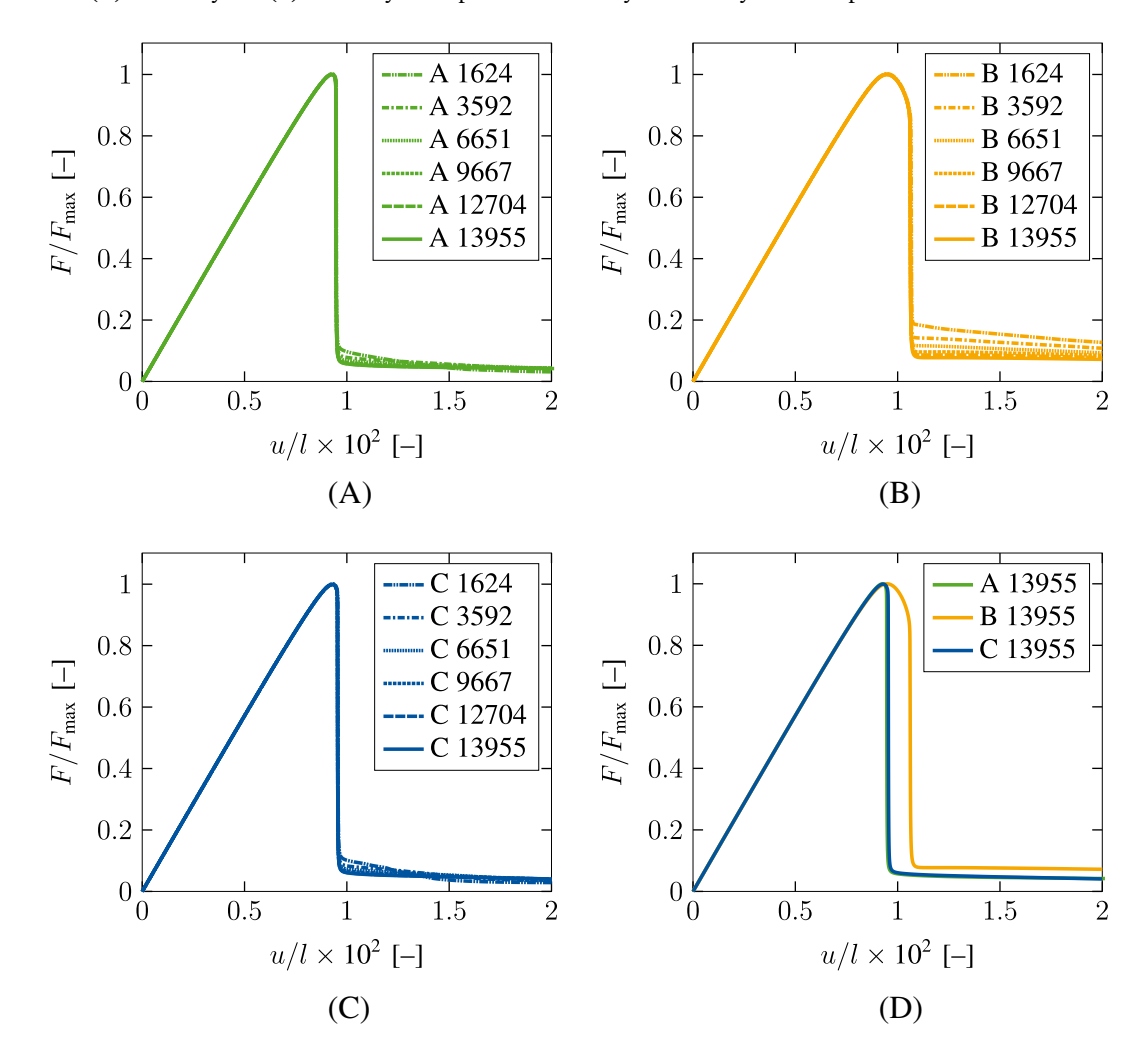


FIGURE 13 Mesh convergence studies for the asymmetrically notched specimen and model comparison. The forces are normalized with respect to the maximum force of the finest mesh (13,955 elements) of model B with $F_{\text{max}} = 3.7959 \times 10^4$ [N]. (A) Model A. (B) Model B. (C) Model C. (D) Model comparison.

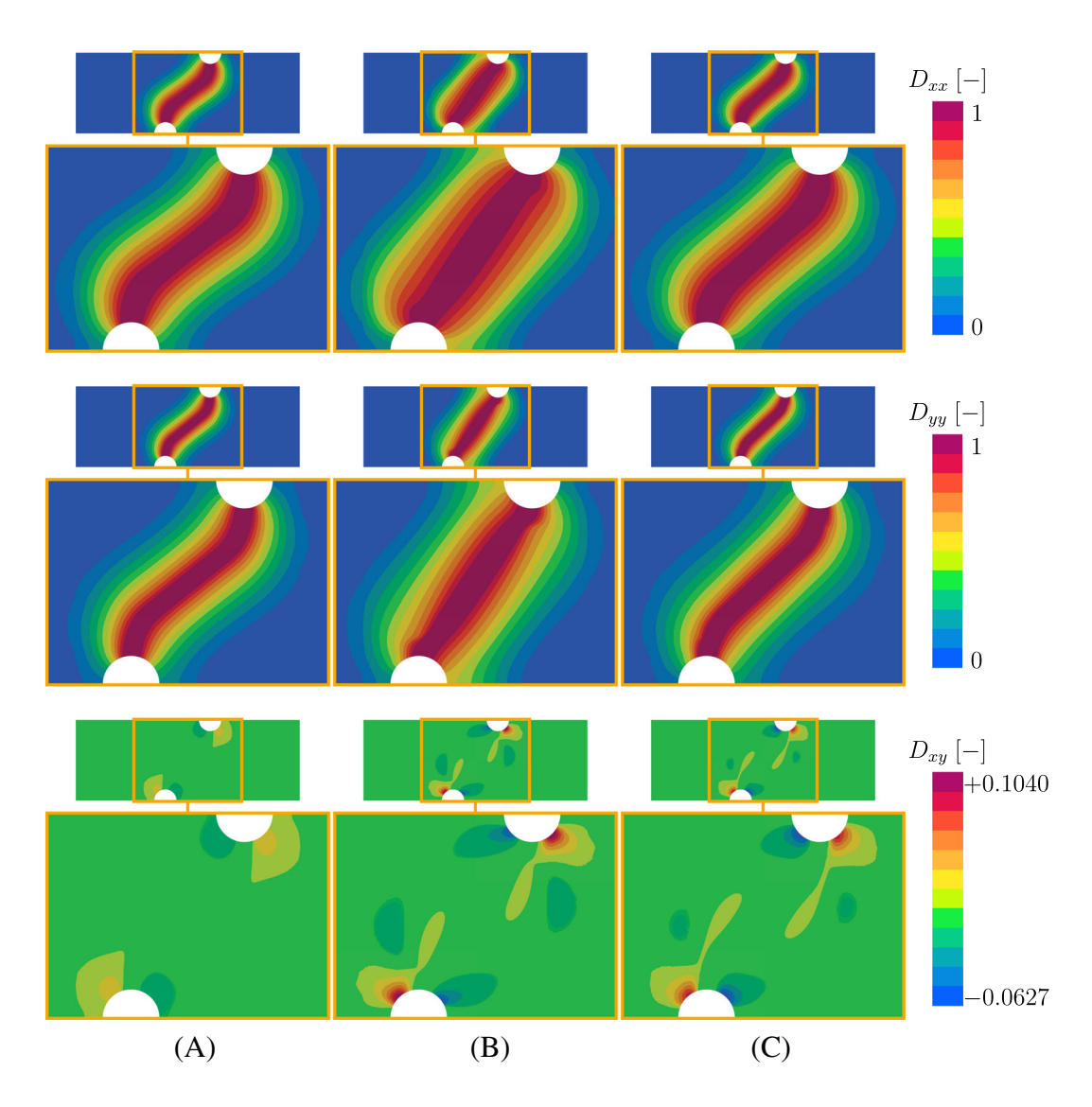


FIGURE 14 Contour plots of the normal and shear components of the damage tensor for the asymmetrically notched specimen at the end of the simulation. (A) Model A. (B) Model B. (C) Model C.

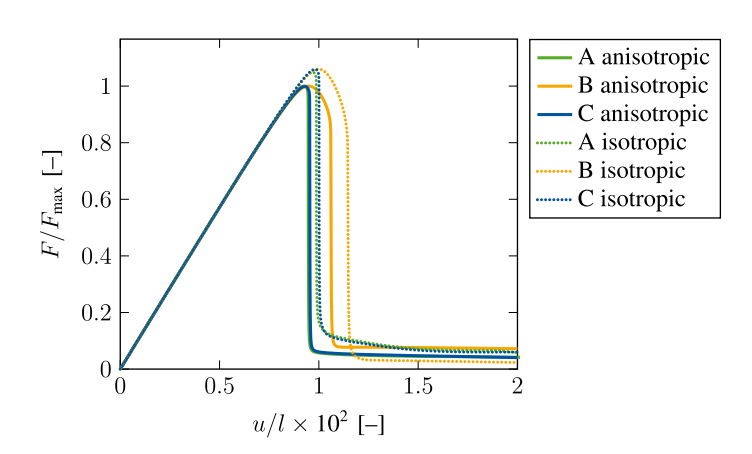


FIGURE 15 Comparison of the anisotropic and isotropic computation for the asymmetrically notched specimen (13,955 elements). The forces are normalized with respect to the maximum force of the anisotropic computation of model B with $F_{\text{max}} = 3.7959 \times 10^4$ [N].

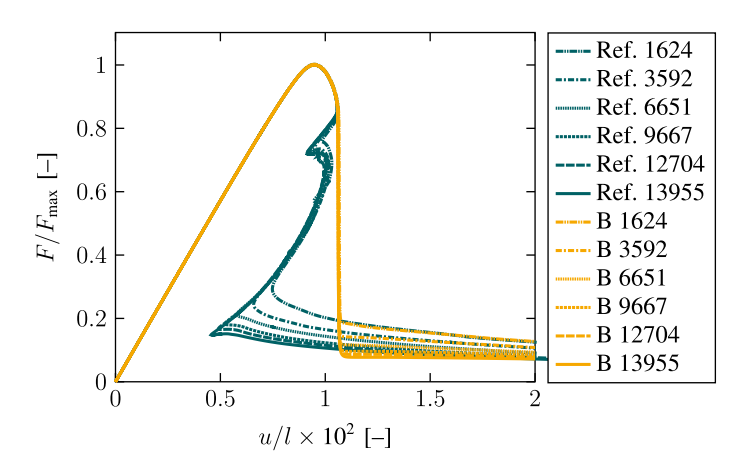


FIGURE 16 Comparison of the results of model B for the asymmetrically notched specimen obtained by a displacement-controlled procedure using artificial viscosity and by an arc-length controlled procedure (reference solution from Holthusen et al.²³). The forces are normalized with respect to the maximum force of the computation with the displacement-driven procedure (13,955 elements) with $F_{\text{max}} = 3.7959 \times 10^4 \text{ [N]}$.

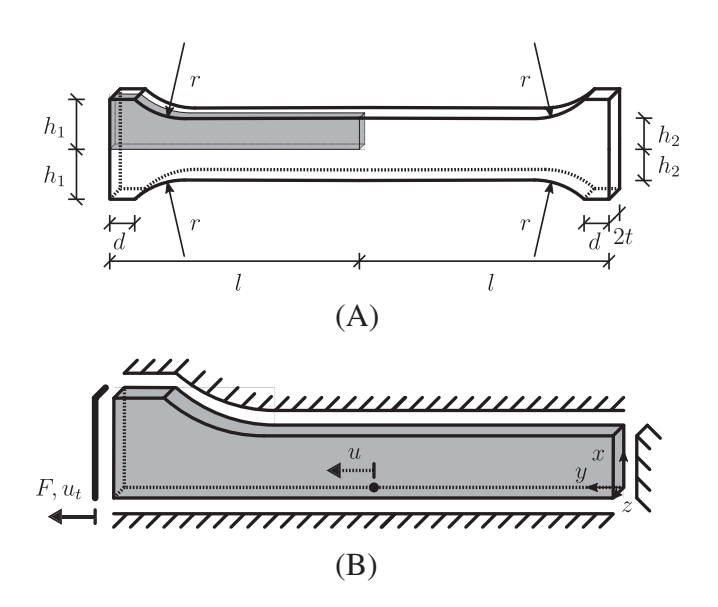


FIGURE 17 (A) Geometry and (B) boundary value problem of the three-dimensional tensile specimen.

4.3 | Three-dimensional tensile specimen

This example features the failure investigation of a three-dimensional I-shaped tensile specimen with models A, B, and C. Previously, this example was investigated in Felder et al.⁷⁶ in the context of thermo-mechanical coupling, in Ambati et al.⁷⁸ numerically and experimentally, and in Holthusen et al.⁶⁷ with a ductile formulation of model B.

Figure 17 shows the geometry and the considered boundary value problem. Due to symmetry, only an eighth of the original specimen is considered in the simulation. The dimensions read l=50 [mm], $h_1=10$ [mm], $h_2=6.25$ [mm], d=5 [mm], r=15 [mm] and t=1.5 [mm]. The three-dimensional finite element meshes stem from Holthusen et al. ⁶⁷ and the mesh with 580 elements contains 996 nodes, the mesh with 4113 elements contains 5788 nodes, the mesh with 13,660 elements contains 16,998 nodes, and the mesh with 18,510 elements contains 22,908 nodes. The internal length scales of model B are chosen as $A_i^{\rm B}=75$ [MPa mm²] and the parameters of model A and C are identified as $A_i^{\rm A}=180$ [MPa mm²] and $A_i^{\rm C}=680$ [MPa mm²]. In the simulation we apply $u_t=2$ [mm] at the end of the specimen and plot in Figure 18 the reaction force F over the displacement u at position x=0 [mm], y=25 [mm], and z=0 [mm] (cf. Figure 17B).

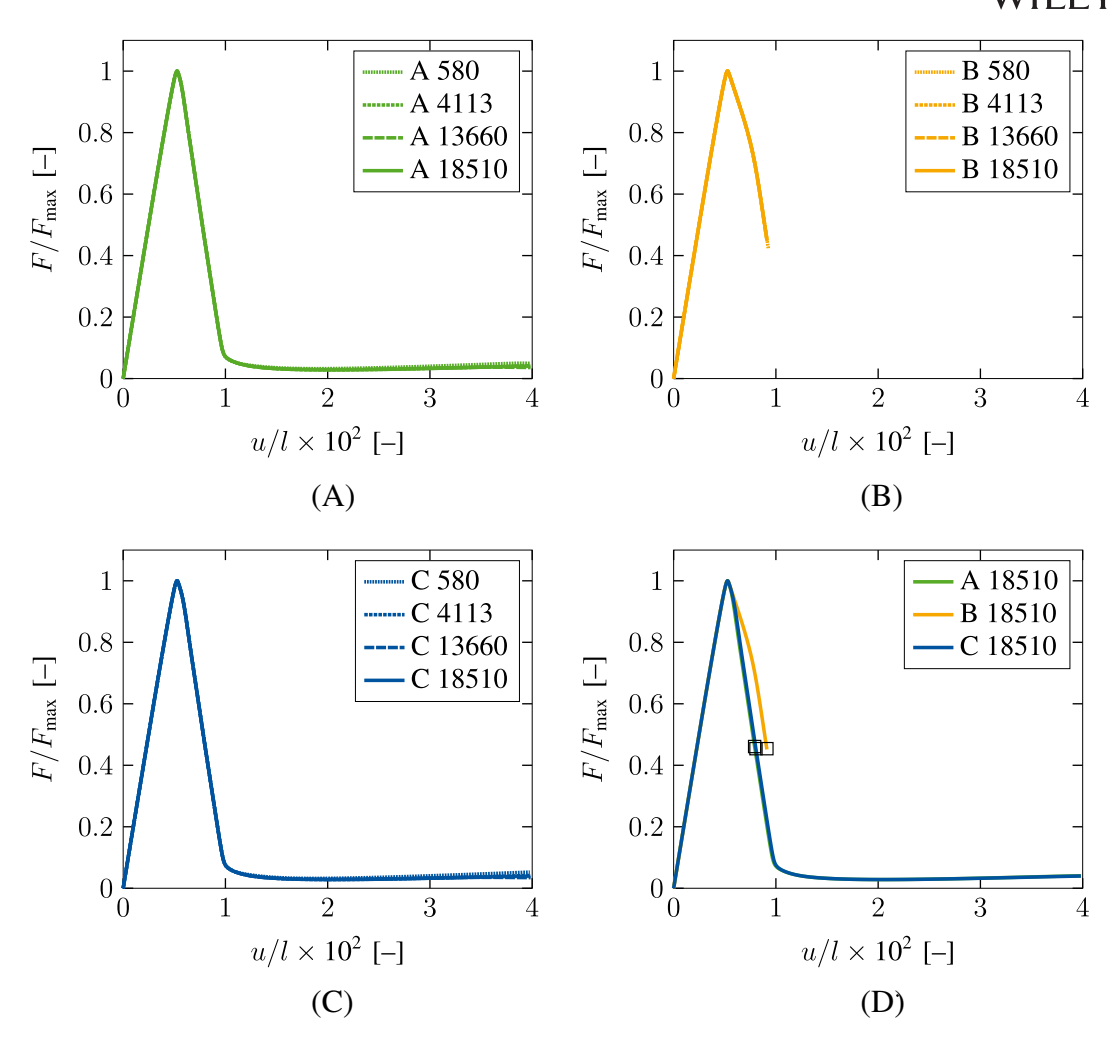


FIGURE 18 Mesh convergence studies for the three-dimensional tensile specimen and model comparison. The forces are normalized with respect to the maximum force of the finest mesh (18,510 elements) of model B with $F_{\text{max}} = 1.1762 \times 10^4$ [N]. The black boxes in (D) indicate the points of comparison in Figures 19 and 20. (A) Model A. (B) Model B. (C) Model C. (D) Model comparison.

In Figure 18, all models again yield in the force-displacement curves the same maximum peak force also for coarse mesh discretizations (580 elements). In this example, only models A and C were able to compute converged solutions up to the final loading of $u_t = 2$ [mm]. With model B, no solution could be obtained due to local convergence problems beyond $u_t = 0.556$ [mm], which corresponds to u = 0.456 [mm] and $u/l \times 10^2 = 0.912$ [–] (see Figure 18B).

The model comparison in Figure 18D shows again an excellent agreement between models A and C, while model B analogously to the previous Sections 4.1 and 4.2, yields a higher energy dissipation. The points of comparison for the damage contour plots in Figures 19 and 20 are indicated by the black boxes in Figure 18D.

As already reported in Holthusen et al.,⁶⁷ the damage tensor component D_{yy} , that is, the degradation of the plane perpendicular to the loading direction evolves most pronounced for all models (see Figure 19). And again, the damage zone of model B spreads furthest and, thus, dissipates the largest amount of energy. Moreover, the contour plots for the normal components agree well for models A and C.

In Figure 20, the study of the shear components D_{xy} , a plane parallel to the loading direction, reveals a concentration at the shoulder of the specimen for all models. The study of the shear components D_{xz} , that is, the plane perpendicular to the loading direction, yields a uniform distribution, except for the center of the specimen with model B. The study of the shear components D_{yz} , that is, the second plane perpendicular to the loading direction, reveals a localization for model B at the transition from the fine to the coarse mesh, which cannot be observed for the full regularization with model A.

FIGURE 19 Contour plots of the normal components of the damage tensor for the three-dimensional tensile specimen at the point of comparison indicated in Figure 18D. (A) Model A. (B) Model B. (C) Model C.

4.4 | Smiley specimen

The final example serves for the investigation of a complex combination of normal and shear stress states. Inspired by Gerke et al.,⁷⁹ Roth and Mohr,⁸⁰ Tancogne-Dejean et al.,⁸¹ Till and Hackl,⁸² and Miyauchi,⁸³ we designed a smiley specimen where the normal and shear load carrying cross sections are equal. The design, further, features smooth transitions from arcs to straight lines to avoid stress singularities at these points. Furthermore, this example illustrates the necessity to investigate the eigenvalues of the damage tensor in order to accurately study the degradation of the specimen and, again, compares the differing results of the isotropic and the anisotropic damage model.

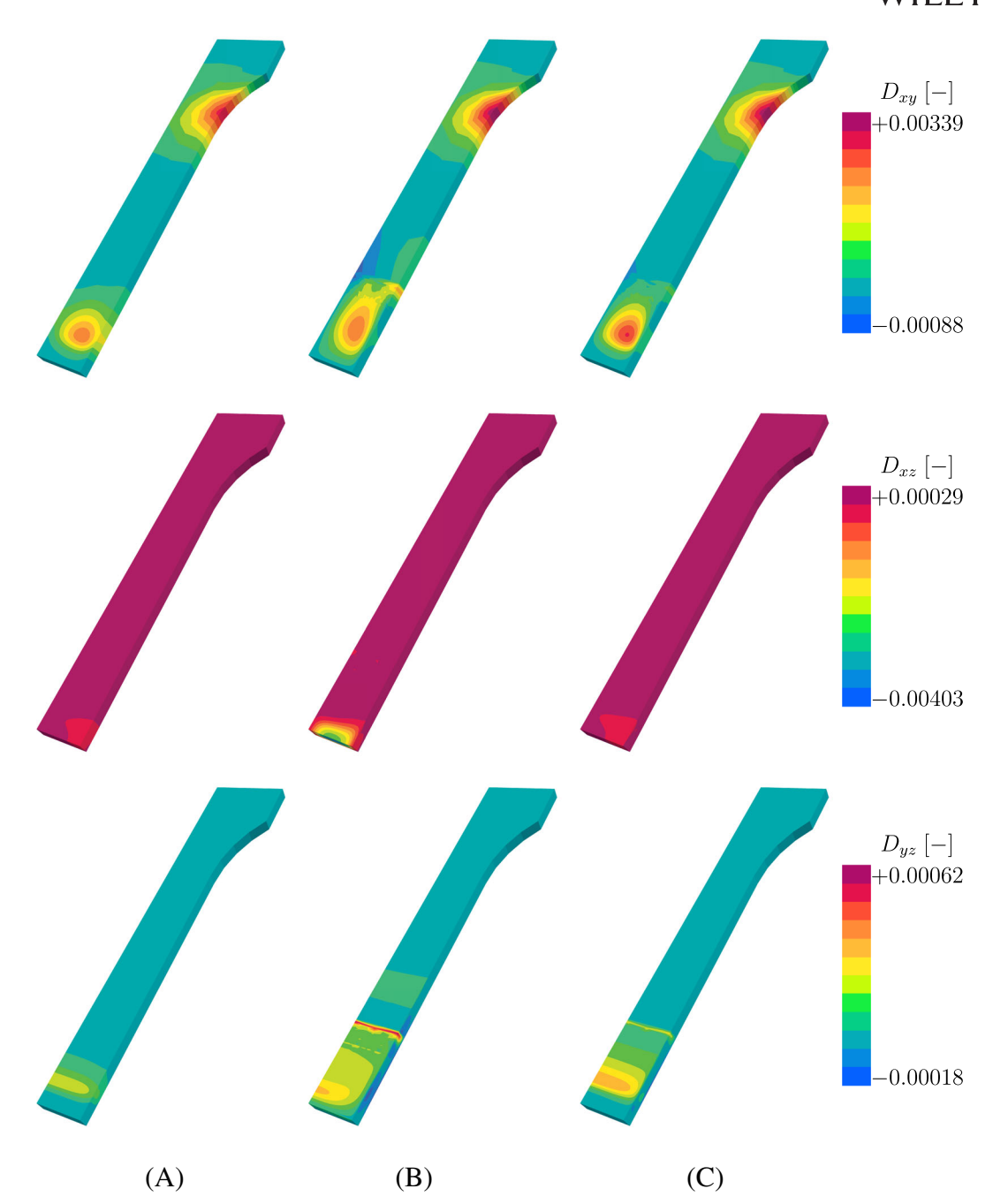


FIGURE 20 Contour plots of the shear components of the damage tensor for the three-dimensional tensile specimen at the point of comparison indicated in Figure 18D. (A) Model A. (B) Model B. (C) Model C.

Figure 21 shows the geometry and the considered boundary value problem. The dimensions read l=50 [mm], $l_1=10$ [mm], $l_2=3.5$ [mm], $l_3=5$ [mm], $l_4=1.5$ [mm], $l_5=4.5$ [mm], $l_6=2$ [mm], $l_7=1$ [mm], $l_8=4$ [mm], w=25 [mm], $w_1=10$ [mm], $w_2=1$ [mm], $w_3=0.5$ [mm], $w_4=4.5$ [mm], $w_5=2$ [mm], $r_1=8$ [mm], $r_2=6.5$ [mm], $r_3=5$ [mm], $r_4=1$ [mm], $r_5=2$ [mm], and $r_6=4$ [mm] with a thickness of 1 [mm]. Due to symmetry, only one half of the specimen with clamped ends is modeled in the simulation. The two-dimensional finite element mesh with 755 elements contains 862 nodes, the mesh with 2649 elements contains 2845 nodes, the mesh with 7681 elements contains 8011 nodes, and the mesh with 13,013 elements contains 13,428 nodes. The internal length scales of model B are chosen as $A_i^B=75$ [MPa mm²] and the parameters of model A and C are identified as $A_i^A=220$ [MPa mm²] and $A_i^C=790$ [MPa mm²].

FIGURE 21 (A) Geometry and (B) boundary value problem of the smiley specimen.

Figure 22 shows the normalized force-displacement curves. In this example, no model obtains convergence with respect to the maximum peak force using the coarsest mesh (755 elements), only upon mesh refinement this is achieved. The model comparison in Figure 22D yields a distinct horizontal offset to the right of the vertical drop for model B at $u_{0.5F_{\rm max}}^{\rm B}/l \times 10^2 = 1.275$ [-]. For this example, a difference in the force drop can also be observed for models A and C with $u_{0.5F_{\rm max}}^{\rm A}/l \times 10^2 = 1.008$ [-] compared to $u_{0.5F_{\rm max}}^{\rm C}/l \times 10^2 = 1.045$ [-]. The damage contour plots in Figure 23 reveal a tension dominated failure with all models, where model B shows the

The damage contour plots in Figure 23 reveal a tension dominated failure with all models, where model B shows the largest damage zone. Moreover, models B and C exhibit concentrated peak values for the shear component of the damage tensor D_{xy} while model A yields a smooth distribution. In Roth and Mohr, 80 a similar geometry is investigated that yields a shear dominated failure, which differs from the tension dominated failure in this work. Due to our specific design of the shear smiley specimen with equal cross sections for tension and shear loads, the failure mode cannot be determined with certainty a priori.

The Green-Lagrange strain components at the end of the simulation are presented in Figure 24. The maximum strain in loading direction yields for model A a value of $E_{yy}^{\rm A}=5.1252$ [-], for model B a value of $E_{yy}^{\rm B}=4.9081$ [-], and for model C a value of $E_{yy}^{\rm C}=4.8018$ [-]. The deformed shapes of the specimen and the strain distributions conform for model A, model B and model C.

For the smiley specimen, we also study the evolution of the components of the damage tensor in Figure 25, where we restrict ourselves to the presentation of model C. In the initial damage state, the normal component D_{xx} evolves equally at the tension and shear load carrying cross sections. In the intermediate damage states, the evolution of D_{xx} concentrates in the normal load carrying cross section up to total failure. The evolution of the normal component D_{yy} occurs predominantly in the normal load carrying cross section during the entire loading. Finally, the evolution of the shear component D_{xy} primarily happens at the inner side of the shear load carrying cross section.

Next, Figure 26 shows the mesh convergence of the components of the damage tensor, where we again restrict ourselves to the presentation of model C. As indicated by the force-displacement curves in Figure 22C, differences can be observed in the damage contour plots obtained with the coarsest mesh (Figure 26A) compared to the results obtained

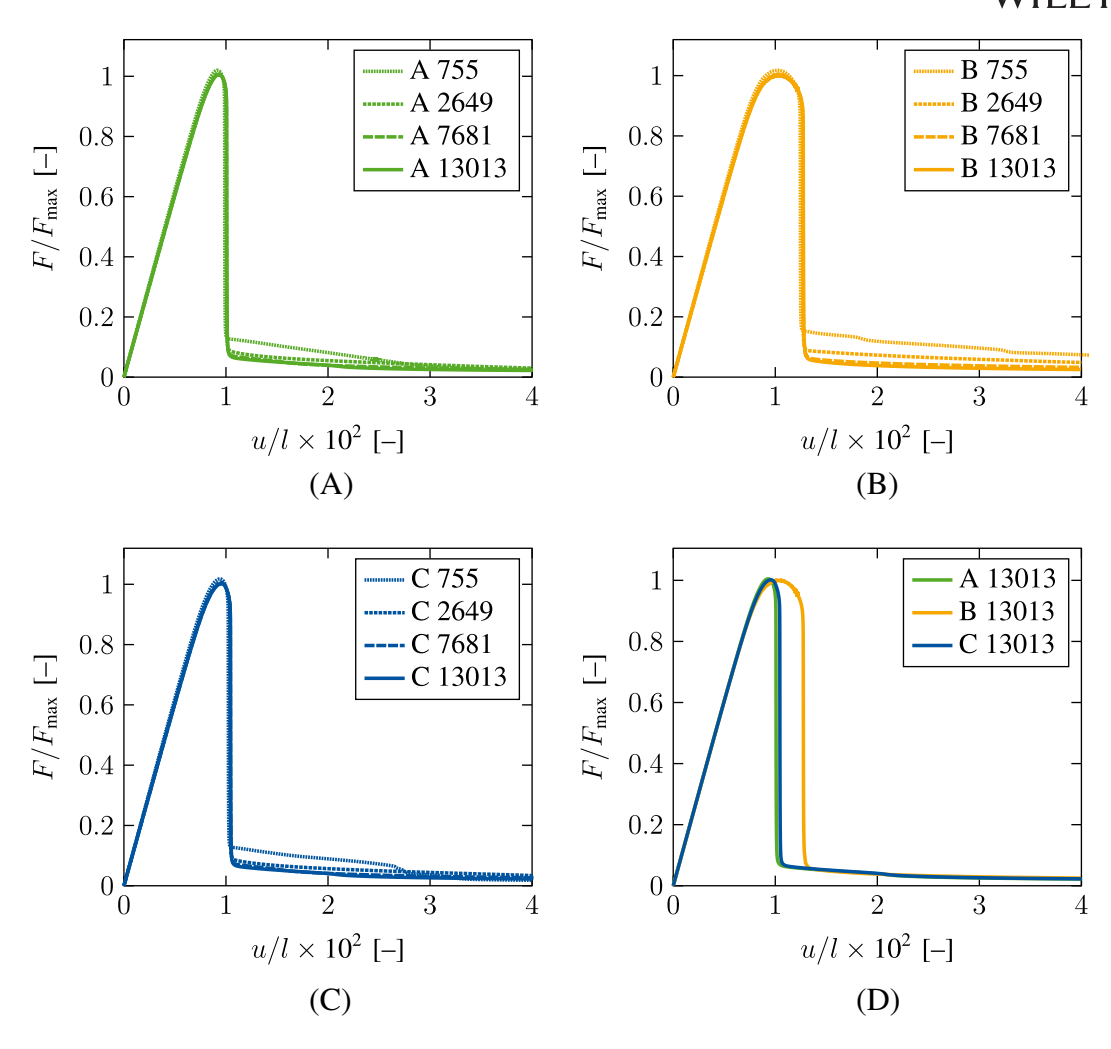


FIGURE 22 Mesh convergence studies for the smiley specimen and model comparison. The forces are normalized with respect to the maximum force of the finest mesh (13,013 elements) of model B with $F_{\text{max}} = 2.9590 \times 10^3$ [N]. (A) Model A. (B) Model B. (C) Model C. (D) Model comparison.

with the refined meshes (Figure 26B–D). However, the results obtained with the refined meshes hardly deviate and are, thus, considered converged.

Now, we study the eigenvalues of the damage tensor for model C. Figure 27 shows the first eigenvalue D_1 (top) and second eigenvalue D_2 (middle) as well as the scaled normals to the corresponding eigenvectors in the x-y-plane. These normals are supposed to indicate the orientation and the density of the anisotropic micro cracks. Hence, the micro cracks associated with the largest eigenvalue D_1 are perpendicular to the loading direction and exhibit the highest density in the completely damaged zone. Due to the orthogonality of eigenvectors and an in-plane loading, the micro cracks associated with the second eigenvalue D_2 are perpendicular to the micro cracks associated with the first eigenvalue D_1 .

Finally, Figure 27 (bottom) shows the difference between the maximum of the normal components D_{xx} , D_{yy} , and D_{zz} and the largest eigenvalue D_1 . Evidently, a significant underestimation of the material degradation up to a value of -0.1926 [-] occurs in the shear load dominated regions, when only considering the normal components of the Cartesian coordinate system.

The last study is concerned with the comparison of isotropic and anisotropic damage for the smiley specimen. Figure 28 shows the normalized force-displacement curves for the isotropic and anisotropic models and for all models the isotropic formulation overestimates the maximum peak force (A: +4.52 [%], B: +9.49 [%], C: +7.65 [%]).

1097(207, 0, Downloaded from https://onlinelibrary.wiley.com/doi/10.1002/nme.7380 by Rwth Aachen Hochschulbibliothek, Wiley Online Library on [15/08/2024]. See the Terms and Condit

onditions) on Wiley Online Library for rules of use; OA articles are governed by the applicable Creative Commons License

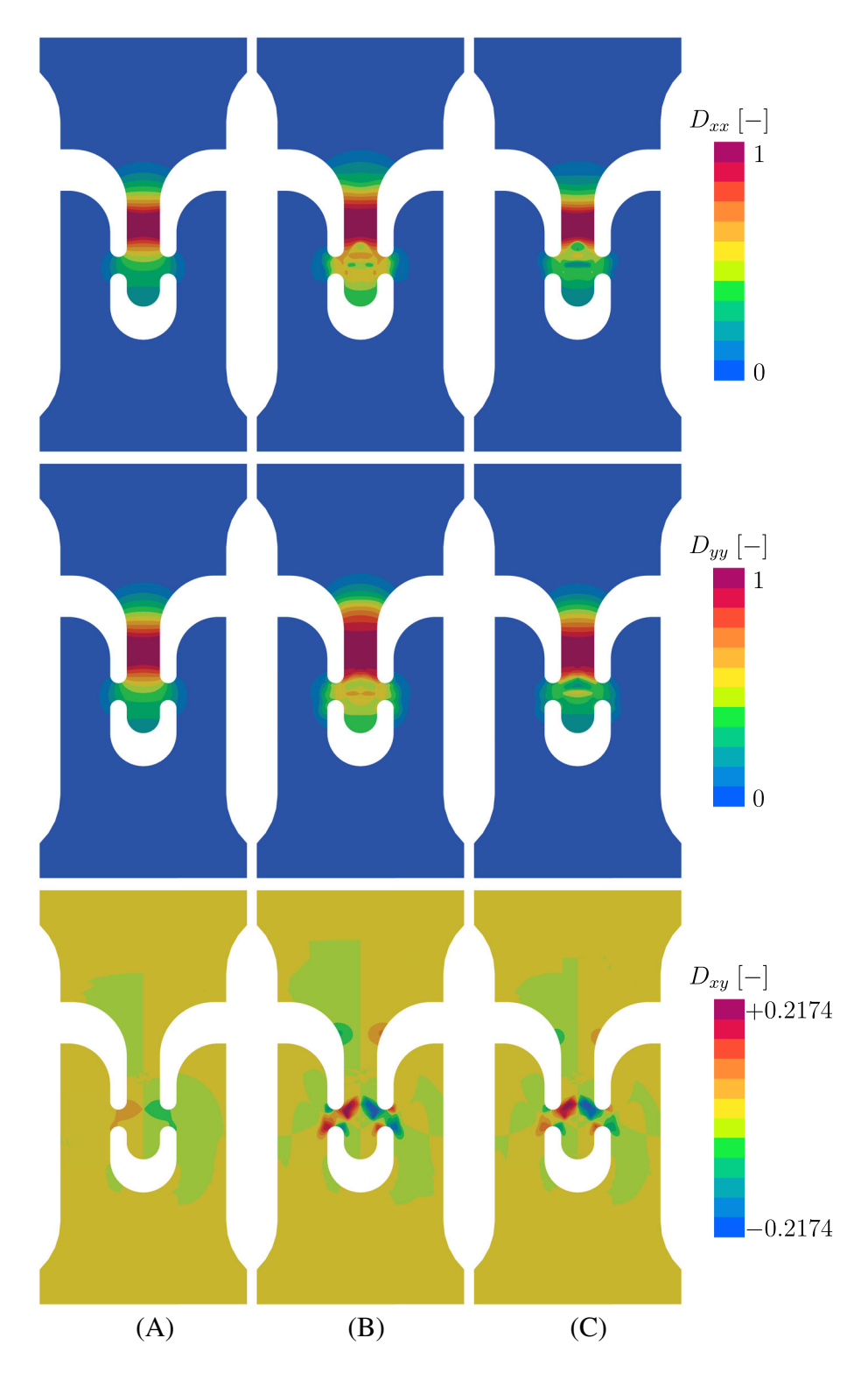


FIGURE 23 Contour plots of the normal and shear components of the damage tensor for the smiley specimen at the end of the simulation. (A) Model A. (B) Model B. (C) Model C.

10970207, 0, Downloaded from https://onlinelibrary.wiley.com/doi/10.1002/nme.7580 by Rwth Aachen Hochschulbibliothek, Wiley Online Library on [15/08/2024]. See the Terms and Conditions (https://onlinelibrary.wiley.

conditions) on Wiley Online Library for rules of use; OA articles are governed by the applicable Creative Commons License

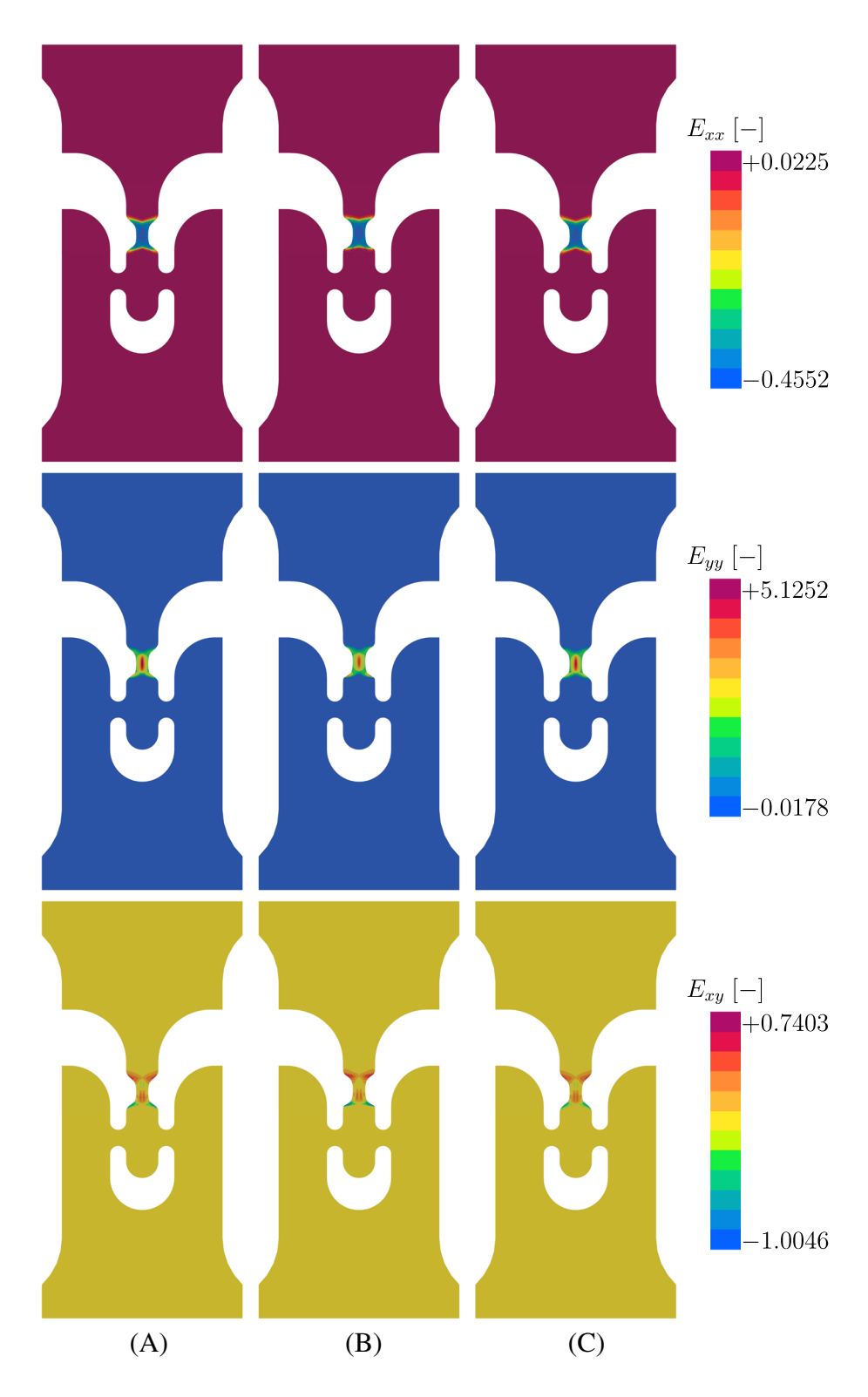


FIGURE 24 Contour plots of the normal and shear components of the Green-Lagrange strain tensor for the smiley specimen at the end of the simulation on the deformed configuration. (A) Model A. (B) Model B. (C) Model C.

FIGURE 25 Contour plots of the evolution of the normal and shear components of the damage tensor for the smiley specimen (model C).

The corresponding isotropic damage contour plots are presented in Figure 29 (top row) and, also for the isotropic models, total failure occurs in the tension load carrying cross section. However, the absolute difference of the isotropic damage value to the normals components of the damage tensor for the anisotropic computation (see Figure 29 (middle and bottom row)) amounts up to 0.4158 [–] for $|D - D_{xx}|$ and to 0.3293 [–] for $|D - D_{yy}|$, which is in line with the observations in Figure 28.

Last, the absolute difference of the isotropic damage value and the largest eigenvalue of the damage tensor for the anisotropic calculation for model C is shown in Figure 30. The value of $|D - D_1|$ reaches up to 0.1581 [-] and, thus, underlines the significant difference between isotropic and anisotropic damage.

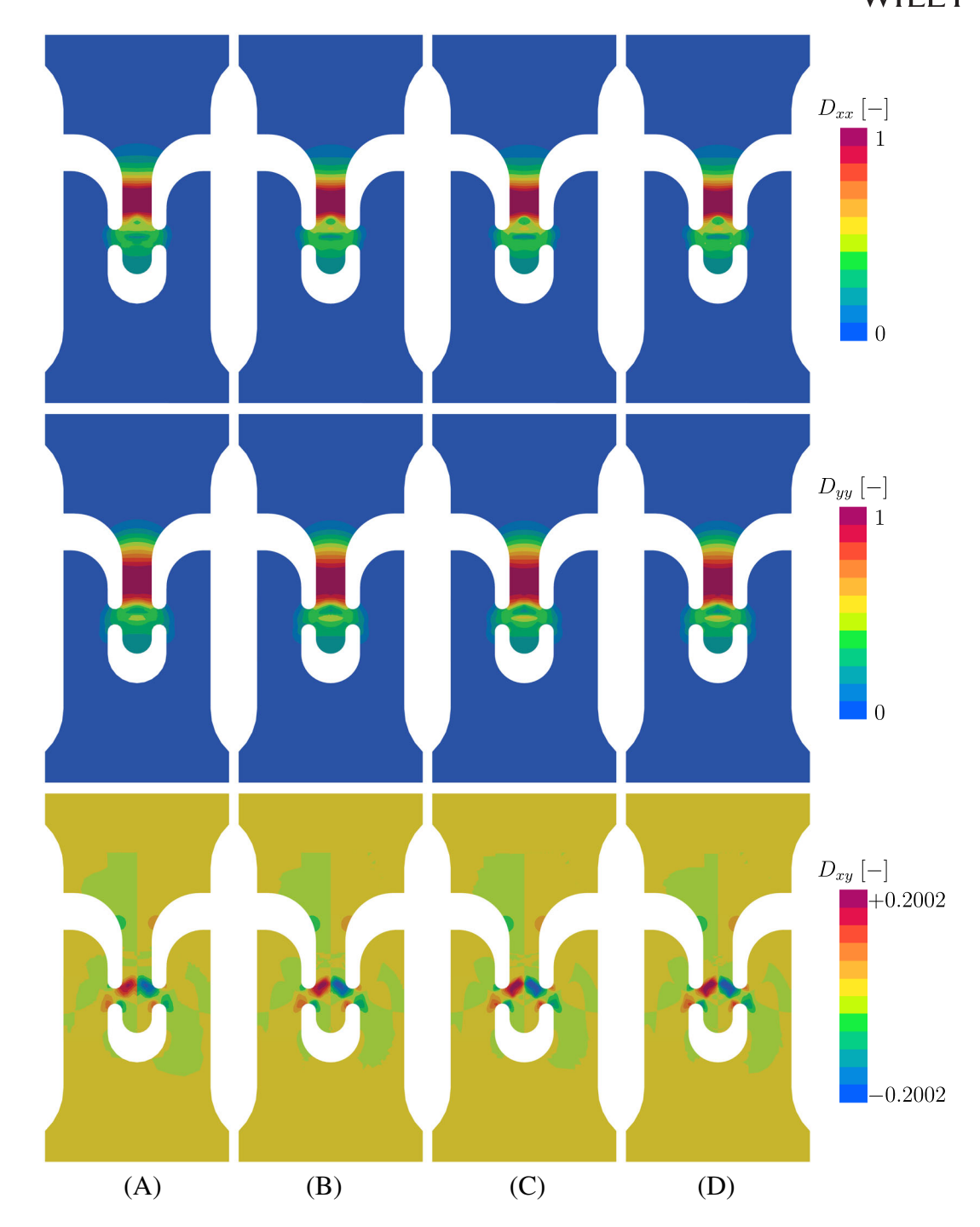


FIGURE 26 Mesh convergence study of the damage contour plots of the normal and shear components of the damage tensor for the smiley specimen at the end of the simulation (model C). (A) 755. (B) 2649. (C) 7681. (D) 13,013.

4.5 | Summary of the numerical results

The following most important results were obtained for model A (full regularization, six micromorphic degrees of freedom), model B (reduced regularization, three micromorphic degrees of freedom), and model C (reduced regularization, two micromorphic degrees of freedom) in the numerical examples:

• Models A, B and C effectively prevent localization in the structural force-displacement response (Figures 2,13,18, and 22).

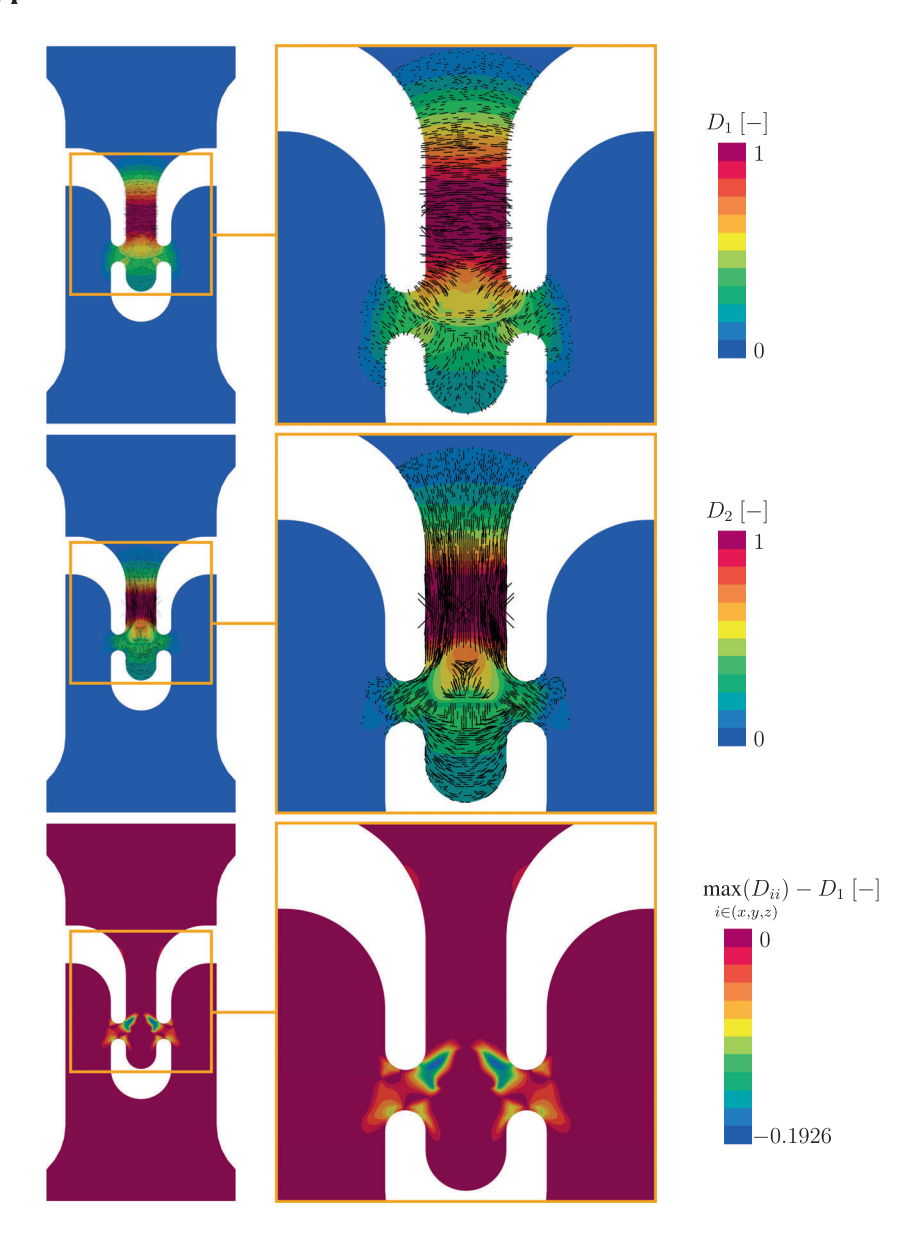


FIGURE 27 Contour plots of the first and second eigenvalue of the damage tensor and of the absolute difference between the maximum normal component and the first eigenvalue for the smiley specimen at the end of the simulation (model C). The black lines indicate the scaled normals to the first (top) and second eigenvector (middle) of the damage tensor.

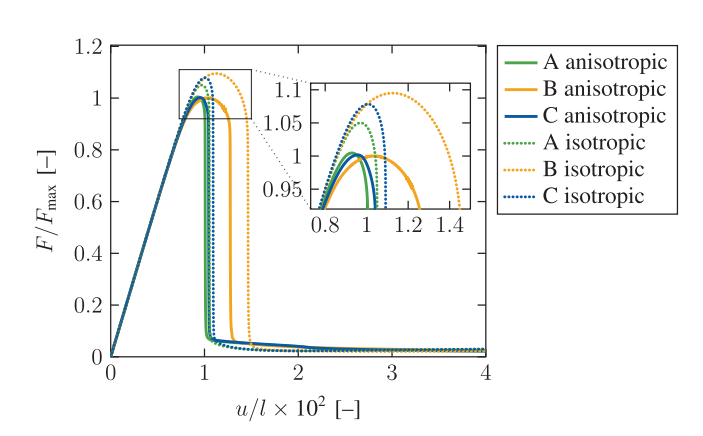


FIGURE 28 Comparison of the anisotropic and isotropic computation for the smiley specimen (13,013 elements). The forces are normalized with respect to the maximum force of the anisotropic computation of model B with $F_{\text{max}} = 2.9590 \times 10^3$ [N].

ditions) on Wiley Online Library for rules of use; OA articles are governed by the applicable Creative Commons License

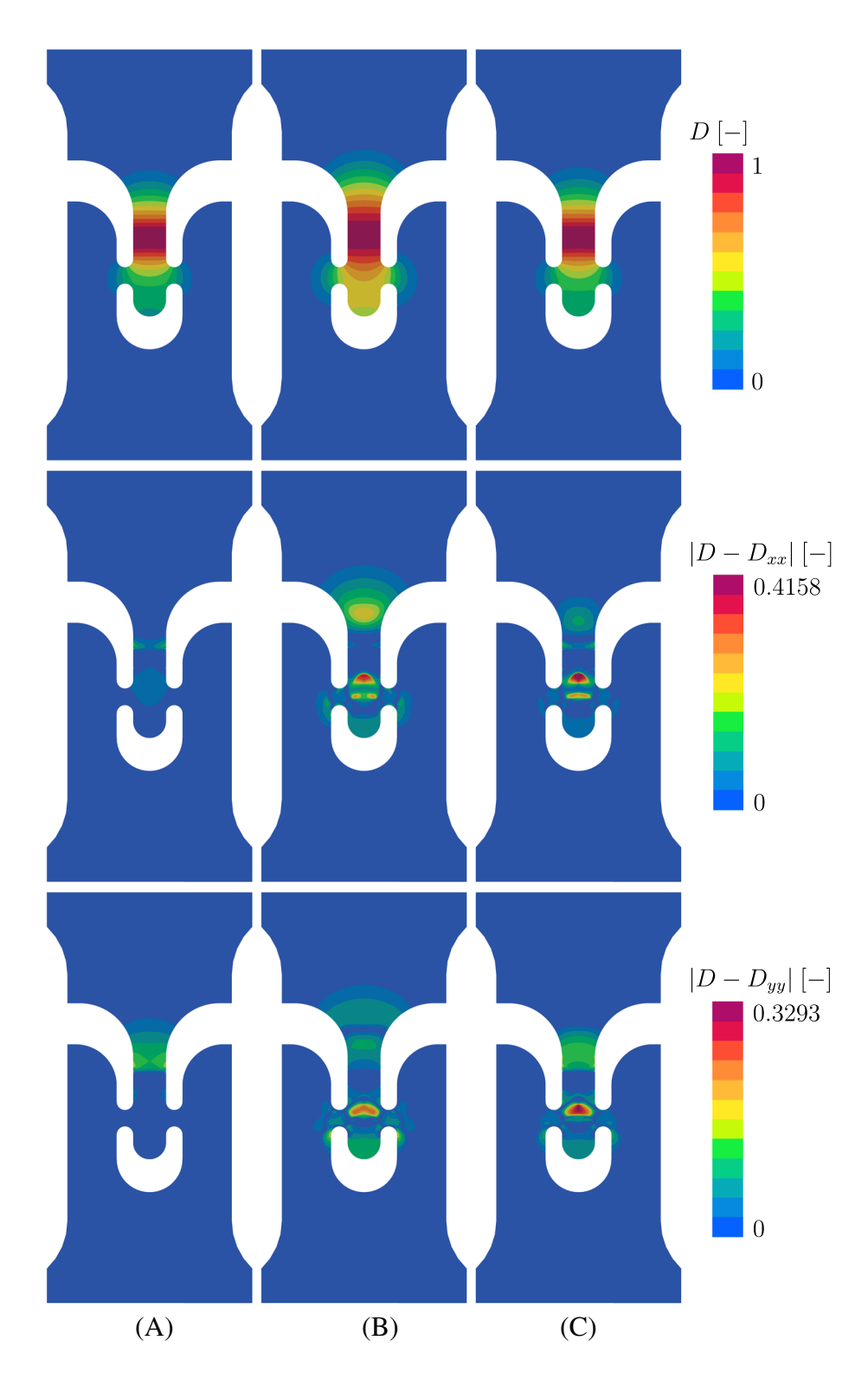


FIGURE 29 Contour plots of the isotropic damage value and its absolute difference to the normal components of the damage tensor for the smiley specimen at the end of the simulation. (A) Model A. (B) Model B. (C) Model C.

FIGURE 30 Contour plot of the absolute difference between the isotropic damage value and the first eigenvalue of the damage tensor for the smiley specimen at the end of the simulation (model C).

- Models A and C coincide in the structural response, while model B yields a higher energy dissipation and a horizontal offset of the vertical force drop to the right for the same maximum peak load (Figures 2D, 13D, 18D, and 22D).
- Models A and C prevent localization of the normal and shear components of the damage tensor (Figures 3A,C, 14A,C, 19A,C, 20A,C, and 23A,C). Model B also prevents localization of the normal components of the damage tensor (Figures 3B, 14B, 19B, and 23B), but a localization of one shear component occurred in a single example (Figure 20B).
- The damage zones obtained with model B are thicker and, thus, dissipate more energy than the damage zones obtained with models A and C (Figures 3,14,19, and 23).
- The consideration of isotropic damage continuously yields an overestimation of the structure's load bearing capacity (Figures 5,15, and 28).
- The influence of the artificial viscosity on the regularization, the structural response, and the damage distribution is ruled out (Figures 7–10 and 16).

5 | CONCLUSION

This work investigated different gradient-extensions for tensor-valued internal variable based inelastic material models. Here, we specifically focused on the regularization of anisotropic damage at finite strains through a micromorphic gradient-extension of the damage driving force. Three different gradient-extensions with full (six micromorphic degrees of freedom) and reduced regularization (three and two micromorphic degrees of freedom) of the damage tensor were compared theoretically and numerically in the present study.

A high level of agreement was obtained between the results of the model with full regularization of all six independent components of the damage tensor and the model with a reduced regularization of the volumetric and deviatoric part of the damage tensor, which only utilizes two micromorphic degrees of freedom. Thereby, an efficient, yet effective, regularization for anisotropic damage at finite strains was identified.

The utilized anisotropic damage model features a flexible formulation that incorporates isotropic, kinematic, and distortional damage hardening and fulfills the damage growth criterion for finite strains. Therefore, it can be considered as a general inelastic local material model of a tensor-valued internal variable based formulation.

Further investigations should verify the numerical results by experimental validations and could apply the gradient-extensions to the regularization of other inelastic localizing phenomena. Moreover, the influence of the micromorphic internal length scale and penalty parameters should be further investigated with respect to the crack width, the numerical costs, and the congruence of the micromorphic nonlocal and local tuples. Finally, the capabilities of a gradient-extension with a single micromorphic degree of freedom could be investigated.

ACKNOWLEDGMENTS

Funding granted by the German Research Foundation (DFG) for projects number 453715964 (RE 1057/51-1), 417002380 (CRC 280 - A01), and 453596084 (CRC 339 - B05) is gratefully acknowledged. Open Access funding enabled and organized by Projekt DEAL.

DATA AVAILABILITY STATEMENT

The data that support the findings of this study are available from the corresponding author upon reasonable request.

ORCID

Tim van der Velden b https://orcid.org/0000-0001-8054-5091

Tim Brepols https://orcid.org/0000-0002-1039-1776

Stefanie Reese https://orcid.org/0000-0003-4760-8358

Hagen Holthusen https://orcid.org/0000-0002-0700-8027

REFERENCES

- 1. de Borst R, Pamin J, Geers M. On coupled gradient-dependent plasticity and damage theories with a view to localization analysis. *Eur J Mech A Solids*. 1999;18(6):939-962.
- 2. Steif P, Spaepen F, Hutchinson J. Strain localization in amorphous metals. Acta Metall. 1982;30(2):447-455.
- 3. Poh L, Peerlings R, Geers M, Swaddiwudhipong S. An implicit tensorial gradient plasticity model—formulation and comparison with a scalar gradient model. *Int J Solids Struct*. 2011;48(18):2595-2604.
- 4. Friedlein J, Mergheim J, Steinmann P. Efficient gradient enhancements for plasticity with ductile damage in the logarithmic strain space. *Eur J Mech A Solids*. 2023:99:104946.
- 5. Carol I, Rizzi E, Willam K. An 'extended' volumetric/deviatoric formulation of anisotropic damage based on a pseudo-log rate. *Eur J Mech A Solids*. 2002;21(5):747-772.
- 6. Leukart M, Ramm E. A comparison of damage models formulated on different material scales. Comput Mater Sci. 2003;28(3):749-762.
- 7. Carol I, Bažant ZP, Prat PC. Geometric damage tensor based on microplane model. J Eng Mech. 1991;117(10):2429-2448.
- 8. Kuhl E, Ramm E, de Borst R. An anisotropic gradient damage model for quasi-brittle materials. *Comput Methods Appl Mech Eng.* 2000;183(1):87-103.
- 9. Voyiadjis GZ, Park T. The kinematics of damage for finite-strain elasto-plastic solids. Int J Eng Sci. 1999;37(7):803-830.
- 10. Schütte H, Bruhns O. On a geometrically nonlinear damage model based on a multiplicative decomposition of the deformation gradient and the propagation of microcracks. *J Mech Phys Solids*. 2002;50(4):827-853.
- 11. Dorn C, Wulfinghoff S. A gradient-extended large-strain anisotropic damage model with crack orientation director. *Comput Methods Appl Mech Eng.* 2021;387:114123.
- 12. Menzel A, Ekh M, Steinmann P, Runesson K. Anisotropic damage coupled to plasticity: modelling based on the effective configuration concept. *Int J Numer Methods Eng.* 2002;54(10):1409-1430.
- 13. Langenfeld K, Mosler J. A micromorphic approach for gradient-enhanced anisotropic ductile damage. *Comput Methods Appl Mech Eng.* 2020;360:112717.
- 14. Sprave L, Menzel A. A large strain anisotropic ductile damage model—effective driving forces and gradient-enhancement of damage vs. plasticity. *Comput Methods Appl Mech Eng.* 2023;416:116284.
- 15. Desmorat R, Gatuingt F, Ragueneau F. Nonlocal anisotropic damage model and related computational aspects for quasi-brittle materials. *Eng Fract Mech.* 2007;74(10):1539-1560.
- 16. Jirásek M, Suárez F. Localization properties of Desmorat's anisotropic damage model. Comput Struct. 2016;174:139-153.
- 17. Badreddine H, Saanouni K, Nguyen TD. Damage anisotropy and its effect on the plastic anisotropy evolution under finite strains. *Int J Solids Struct*. 2015;63:11-31.
- 18. Desmorat R. Anisotropic damage modeling of concrete materials. Int J Damage Mech. 2016;25(6):818-852.
- 19. Fassin M, Eggersmann R, Wulfinghoff S, Reese S. Efficient algorithmic incorporation of tension compression asymmetry into an anisotropic damage model. *Comput Methods Appl Mech Eng.* 2019;354:932-962.
- 20. Fassin M, Eggersmann R, Wulfinghoff S, Reese S. Gradient-extended anisotropic brittle damage modeling using a second order damage tensor—theory, implementation and numerical examples. *Int J Solids Struct*. 2019;167:93-126.
- 21. Reese S, Brepols T, Fassin M, Poggenpohl L, Wulfinghoff S. Using structural tensors for inelastic material modeling in the finite strain regime—a novel approach to anisotropic damage. *J Mech Phys Solids*. 2021;146:104174.
- 22. Hegde M, Mulay SS. Evolving structural tensor approach to model the damage induced anisotropy in viscoelastic solids. *Int J Solids Struct*. 2022;248:111655.
- 23. Holthusen H, Brepols T, Reese S, Simon J-W. A two-surface gradient-extended anisotropic damage model using a second order damage tensor coupled to additive plasticity in the logarithmic strain space. *J Mech Phys Solids*. 2022;163:104833.
- 24. Pijaudier-Cabot G, Bažant ZP. Nonlocal damage theory. J Eng Mech. 1987;113(10):1512-1533.
- 25. Bažant ZP, Pijaudier-Cabot G. Nonlocal continuum damage, localization instability and convergence. J Appl Mech. 1988;55(2):287-293.
- 26. Bažant ZP, Jirásek M. Nonlocal integral formulations of plasticity and damage: survey of progress. J Eng Mech. 2002;128(11):1119-1149.

- 27. Needleman A. Material rate dependence and mesh sensitivity in localization problems. Comput Methods Appl Mech Eng. 1988;67(1):69-85.
- 28. Geers MGD, Brekelmans WAM, de Borst R. Viscous regularization of strain-localisation for damaging materials. *DIANA Computational Mechanics*'94. Springer; 1994:127-138.
- 29. Niazi MS, Wisselink HH, Meinders T. Viscoplastic regularization of local damage models: revisited. Comput Mech. 2013;51:203-216.
- 30. Langenfeld K, Junker P, Mosler J. Quasi-brittle damage modeling based on incremental energy relaxation combined with a viscous-type regularization. *Contin Mech Thermodyn.* 2018;30(5):1125-1144.
- 31. Silling S. Reformulation of elasticity theory for discontinuities and long-range forces. J Mech Phys Solids. 2000;48(1):175-209.
- 32. Javili A, McBride AT, Steinmann P. A geometrically exact formulation of peridynamics. Theor Appl Fract Mech. 2021;111:102850.
- 33. Laurien M, Javili A, Steinmann P. Peridynamic modeling of nonlocal degrading interfaces in composites. Forces Mech. 2023;10:100124.
- 34. Peerlings RHJ, de Borst R, Brekelmans WAM, de Vree JHP. Gradient enhanced damage for quasi-brittle materials. *Int J Numer Methods Eng.* 1996;39(19):3391-3403.
- 35. de Borst R, Benallal A, Heeres O. A gradient-enhanced damage approach to fracture. J Phys IV Proc. 1996;6:491-502.
- 36. Dimitrijevic BJ, Hackl K. A method for gradient enhancement of continuum damage models. Tech Mech Eur J Eng Mech. 2008;28(1):43-52.
- 37. Dimitrijevic BJ, Hackl K. A regularization framework for damage-plasticity models via gradient enhancement of the free energy. *Int J Numer Method Biomed Eng.* 2011;27(8):1199-1210.
- 38. Forest S. Micromorphic approach for gradient elasticity, viscoplasticity, and damage. J Eng Mech. 2009;135(3):117-131.
- 39. Forest S. Nonlinear regularization operators as derived from the micromorphic approach to gradient elasticity, viscoplasticity and damage. *Proc R Soc A Math Phys Eng Sci.* 2016;472(2188):20150755.
- 40. Wulfinghoff S, Böhlke T. Equivalent plastic strain gradient enhancement of single crystal plasticity: theory and numerics. *Proc R Soc A Math Phys Eng Sci.* 2012;468(2145):2682-2703.
- 41. Wulfinghoff S, Forest S, Böhlke T. Strain gradient plasticity modeling of the cyclic behavior of laminate microstructures. *J Mech Phys Solids*. 2015;79:1-20.
- 42. Jebahi M, Forest S. Scalar-based strain gradient plasticity theory to model size-dependent kinematic hardening effects. *Contin Mech Thermodyn.* 2021;33:1223-1245.
- 43. Abatour M, Forest S, Ammar K, Ovalle C, Osipov N, Quilici S. Toward robust scalar-based gradient plasticity modeling and simulation at finite deformations. *Acta Mech.* 2023;234:911-958.
- 44. Abatour M, Forest S. Strain gradient plasticity based on saturating variables. Eur J Mech A Solids. 2023;104:105016.
- 45. Holthusen H, Brepols T, Reese S, Simon J-W. An anisotropic constitutive model for fiber-reinforced materials including gradient-extended damage and plasticity at finite strains. *Theor Appl Fract Mech.* 2020;108:102642.
- 46. Poggenpohl L, Brepols T, Holthusen H, Wulfinghoff S, Reese S. Towards brittle damage in carbon fiber reinforced plastics: a gradient extended approach. *Compos Struct*. 2021;255:112911.
- 47. Poggenpohl L, Holthusen H, Simon J-W. Failure zone homogenization for modeling damage- and debonding-induced softening in composites including gradient-extended damage at finite strains. *Int J Plast*. 2022;154:103277.
- 48. Langenfeld K, Kurzeja P, Mosler J. How regularization concepts interfere with (quasi-)brittle damage: a comparison based on a unified variational framework. *Contin Mech Thermodyn.* 2022;34:1517-1544.
- 49. Aldakheel F, Hudobivnik B, Wriggers P. Virtual element formulation for phase-field modeling of ductile fracture. *Int J Multiscale Comput Eng.* 2019;17(2):181-200.
- 50. Barfusz O, van der Velden T, Brepols T, Holthusen H, Reese S. A reduced integration-based solid-shell finite element formulation for gradient-extended damage. *Comput Methods Appl Mech Eng.* 2021;382:113884.
- 51. Barfusz O, van der Velden T, Brepols T, Reese S. Gradient-extended damage analysis with reduced integration-based solid-shells at large deformations. *Comput Methods Appl Mech Eng.* 2022;389:114317.
- 52. Kikis G, Ambati M, De Lorenzis L, Klinkel S. Phase-field model of brittle fracture in Reissner–Mindlin plates and shells. *Comput Methods Appl Mech Eng.* 2021;373:113490.
- 53. Dittmann M, Aldakheel F, Schulte J, et al. Phase-field modeling of porous-ductile fracture in non-linear thermo-elasto-plastic solids. *Comput Methods Appl Mech Eng.* 2020;361:112730.
- 54. Sarkar S, Singh I, Mishra B. A thermo-mechanical gradient enhanced damage method for fracture. Comput Mech. 2020;66:1399-1426.
- 55. van der Velden T, Ritzert S, Reese S, Waimann J. A novel numerical strategy for modeling the moving boundary value problem of electrochemical machining. *Int J Numer Methods Eng.* 2023;124(8):1856-1882.
- 56. van der Velden T, Rommes B, Klink A, Reese S, Waimann J. A novel approach for the efficient modeling of material dissolution in electrochemical machining. *Int J Solids Struct*. 2021;229:111106.
- 57. Holthusen H, Lamm L, Brepols T, Reese S, Kuhl E. Theory and implementation of inelastic constitutive artificial neural networks. *Comput Methods Appl Mech Eng.* 2024;428:117063.
- 58. Wulfinghoff S, Fassin M, Reese S. A damage growth criterion for anisotropic damage models motivated from micromechanics. *Int J Solids Struct.* 2017;121:21-32.
- 59. Miehe C, Apel N, Lambrecht M. Anisotropic additive plasticity in the logarithmic strain space: modular kinematic formulation and implementation based on incremental minimization principles for standard materials. *Comput Methods Appl Mech Eng.* 2002;191(47):5383-5425.
- 60. Hansen N, Schreyer H. A thermodynamically consistent framework for theories of elastoplasticity coupled with damage. *Int J Solids Struct*. 1994;31(3):359-389.
- 61. Coleman BD, Noll W. Foundations of linear viscoelasticity. Rev Mod Phys. 1961;33:239-249.
- 62. Lemaitre J, Desmorat R, Sauzay M. Anisotropic damage law of evolution. Eur J Mech A Solids. 2000;19(2):187-208.

- 63. Simo J. On a fully three-dimensional finite-strain viscoelastic damage model: formulation and computational aspects. *Comput Methods Appl Mech Eng.* 1987;60(2):153-173.
- 64. Challamel N, Lanos C, Casandjian C. Strain-based anisotropic damage modelling and unilateral effects. Int J Mech Sci. 2005;47(3):459-473.
- 65. Korelc J. Multi-language and multi-environment generation of nonlinear finite element codes. Eng Comput. 2002;18:312-327.
- 66. Korelc J, Wriggers P. Automation of Finite Element Methods. Springer; 2016.
- 67. Holthusen H, Brepols T, Simon J-W, Reese S. A gradient-extended anisotropic damage-plasticity model in the logarithmic strain space. *ECCOMAS Congress 2022: 8th European Congress on Computational Methods in Applied Sciences and Engineering.* Scipedia; 2022:1-12.
- 68. Brepols T, Wulfinghoff S, Reese S. A gradient-extended two-surface damage-plasticity model for large deformations. *Int J Plast*. 2020;129:102635.
- 69. Taylor RL, Govindjee S. FEAP—A Finite Element Analysis Program. University of California, Berkeley; 2020 http://projects.ce.berkeley .edu/feap/manual_86.pdf
- 70. HyperWorks. Hypermesh. Altair Engineering, Inc.; 2022 https://altairhyperworks.com/product/HyperMesh
- 71. Ahrens J, Geveci B, Law C. ParaView: an end-user tool for large data visualization. Visualization Handbook. Elsevier; 2005.
- 72. Friedlein J, Mergheim J, Steinmann P. A finite plasticity gradient-damage model for sheet metals during forming and clinching. *Key Eng Mater*. 2021;883:57-64.
- 73. Sprave L, Menzel A. A large strain gradient-enhanced ductile damage model: finite element formulation, experiment and parameter identification. *Acta Mech.* 2020;231:5159-5192.
- 74. Kiefer B, Waffenschmidt T, Sprave L, Menzel A. A gradient-enhanced damage model coupled to plasticity—multi-surface formulation and algorithmic concepts. *Int J Damage Mech.* 2018;27(2):253-295.
- 75. Brepols T, Wulfinghoff S, Reese S. Gradient-extended two-surface damage-plasticity: micromorphic formulation and numerical aspects. *Int J Plast*. 2017;97:64-106.
- 76. Felder S, Kopic-Osmanovic N, Holthusen H, Brepols T, Reese S. Thermo-mechanically coupled gradient-extended damage-plasticity modeling of metallic materials at finite strains. *Int J Plast*. 2022;148:103142.
- 77. Barfusz O, Brepols T, van der Velden T, Frischkorn J, Reese S. A single Gauss point continuum finite element formulation for gradient-extended damage at large deformations. *Comput Methods Appl Mech Eng.* 2021;373:113440.
- 78. Ambati M, Kruse R, De Lorenzis L. A phase-field model for ductile fracture at finite strains and its experimental verification. *Comput Mech.* 2016;57:149-167.
- 79. Gerke S, Zistl M, Brünig M. Experiments and numerical simulation of damage and fracture of the X0-specimen under non-proportional loading paths. *Eng Fract Mech.* 2020;224:106795.
- 80. Roth CC, Mohr D. Ductile fracture experiments with locally proportional loading histories. Int J Plast. 2016;79:328-354.
- 81. Tancogne-Dejean T, Roth CC, Woy U, Mohr D. Probabilistic fracture of Ti-6Al-4V made through additive layer manufacturing. *Int J Plast*. 2016;78:145-172.
- 82. Till E, Hackl B. Calibration of plasticity and failure models for AHSS sheets. Towards Zero Failure Production Methods by Advanced Modeling Techniques and a Process Integrated Virtual Control, IDDRG, International Deep Drawing Research Group Conference; 2013;119–124.
- 83. Miyauchi K. A proposal for a planar simple shear test in sheet metals. Sci Pap Inst Phys Chem Res (Jpn). 1984;78(3):27-40.

How to cite this article: van der Velden T, Brepols T, Reese S, Holthusen H. A comparative study of micromorphic gradient-extensions for anisotropic damage at finite strains. *Int J Numer Methods Eng.* 2024;e7580. doi: 10.1002/nme.7580